The Astrophysical Journal, 908:10 (20pp), 2021 February 10 https://doi.org/10.3847/1538-4357/abd0fc

Observations of Magnetic Fields Surrounding LkHα 101 Taken by the BISTRO Survey with JCMT-POL-2

Nguyen Bich Ngoc[1], Pham Ngoc Diep[1], Harriet Parsons[2], Kate Pattle[3], Thiem Hoang[4,5], Derek Ward-Thompson[6], Le Ngoc Tram[7], Charles L. H. Hull[8,9,84], Mehrnoosh Tahani[10], Ray Furuya[11], Pierre Bastien[12], Keping Qiu[13], Tetsuo Hasegawa[14], Woojin Kwon[15], Yasuo Doi[16], Shih-Ping Lai[17,18], Simon Coudé[19], David Berry[2], Tao-Chung Ching[20,21], Jihye Hwang[4,5], Archana Soam[19], Jia-Wei Wang[18], Doris Arzoumanian[22], Tyler L. Bourke[23,24], Do-Young Byun[4,5], Huei-Ru Vivien Chen[17,18], Zhiwei Chen[25], Wen Ping Chen[26], Mike Chen[27], Jungyeon Cho[28], Yunhee Choi[4], Minho Choi[4], Antonio Chrysostomou[29], Eun Jung Chung[28], Sophia Dai[21], James Di Francesco[27,30], Yan Duan[21], Hao-Yuan Duan[17], David Eden[31], Chakali Eswaraiah[20,21], Lapo Fanciullo[18], Jason Fiege[32], Laura M. Fissel[33], Erica Franzmann[32], Per Friberg[34], Rachel Friesen[34], Gary Fuller[35], Tim Gledhill[29], Sarah Graves[2], Jane Greaves[36], Matt Griffin[36], Qilao Gu[37], Ilseung Han[4,5], Jennifer Hatchell[38], Saeko Hayashi[39], Martin Houde[40], Tsuyoshi Inoue[41], Shu-ichiro Inutsuka[41], Kazunari Iwasaki[42], Il-Gyo Jeong[4], Doug Johnstone[27,30], Ji-hyun Kang[4], Sung-ju Kang[4], Miju Kang[4], Akimasa Kataoka[43], Koji Kawabata[44,45,46], Francisca Kemper[18,47], Kee-Tae Kim[4,5], Jongsoo Kim[4,5], Tae-Soo Pyo[39,48], Lei Qian[20], Ramprasad Rao[18], Mark Rawlings[2], Jonathan Rawlings[49], Brendan Retter[36], John Richer[50,51], Andrew Rigby[36], Sarah Sadavoy[33], Hiro Saito[52], Giorgio Savini[53], Anna Scaife[35], Masumichi Seta[54], Gwanjeong Kim[55], Shinyoung Kim[4,5], Kyoung Hee Kim[4], Mi-Ryang Kim[4], Florian Kirchschlager[49], Jason Kirk[6], Masato I. N. Kobayashi[56], Patrick M. Koch[18], Vera Konyves[6], Takayoshi Kusune[14], Jungmi Kwon[57], Kevin Lacaille[58,59], Chi-Yan Law[37,60], Sang-Sung Lee[4,5], Yong-Hee Lee[61], Chin-Fei Lee[18], Jeong-Eun Lee[61], Hyeseung Lee[28], Chang Won Lee[4,5], Di Li[62,63], Hua-bai Li[37], Dalei Li[64], Hong-Li Liu[65,66], Junhao Liu[13,67], Tie Liu[68], Sheng-Yuan Liu[18], Xing Lu[69], A-Ran Lyo[4], Steve Mairs[70], Masafumi Matsumura[70], Brenda Matthews[27,30], Gerald Moriarty-Schieven[30], Tetsuya Nagata[71], Fumitaka Nakamura[43,48], Hiroyuki Nakanishi[72], Nagayoshi Ohashi[39], Takashi Onaka[57,73], Geumsook Park[4], Nicolas Peretto[36], Yoshito Shimajiri[14], Hiroko Shinnaga[72], Motohide Tamura[14,57,74], Ya-Wen Tang[18], Xindi Tang[75], Kohji Tomisaka[43,48], Yusuke Tsukamoto[72], Serena Viti[76], Hongchi Wang[77], Anthony Whitworth[36], Jinjin Xie[21], Hsi-Wei Yen[18], Hyunju Yoo[4], Jinghua Yuan[21], Hyeong-Sik Yun[61], Tetsuya Zenko[71], Yapeng Zhang[37], Chuan-Peng Zhang[20,21], Guoyin Zhang[20], Jianjun Zhou[64], Lei Zhu[20], Ilse de Looze[76], Philippe André[78], C. Darren Dowell[79], Stewart Eyres[80], Sam Falle[81], Jean-François Robitaille[82], and Sven van Loo[83]

[1] Vietnam National Space Center, Vietnam Academy of Science and Technology, 18 Hoang Quoc Viet, Hanoi, Vietnam; pndiep@vnsc.org.vn
[2] East Asian Observatory, 660 N. A'ohōkū Place, University Park, Hilo, HI 96720, USA
[3] National University of Ireland Galway, University Road, Galway, H91 TK33, Ireland
[4] Korea Astronomy and Space Science Institute, 776 Daedeokdae-ro, Yuseong-gu, Daejeon 34055, Republic of Korea
[5] University of Science and Technology, Korea, 217 Gajeong-ro, Yuseong-gu, Daejeon 34113, Republic of Korea
[6] Jeremiah Horrocks Institute, University of Central Lancashire, Preston PR1 2HE, UK
[7] University of Science and Technology of Hanoi, Vietnam Academy of Science and Technology, 18 Hoang Quoc Viet, Hanoi, Vietnam
[8] National Astronomical Observatory of Japan, NAOJ Chile, Alonso de Córdova 3788, Office 61B, 7630422, Vitacura, Santiago, Chile
[9] Joint ALMA Observatory, Alonso de Córdova 3107, Vitacura, Santiago, Chile
[10] Dominion Radio Astrophysical Observatory, Herzberg Astronomy and Astrophysics Research Centre, National Research Council Canada, P.O. Box 248, Penticton, BC V2A 6J9 Canada
[11] Institute of Liberal Arts and Sciences Tokushima University, Minami Jousanajima-machi 1-1, Tokushima 770-8502, Japan
[12] Centre de recherche en astrophysique du Québec & département de physique, Université de Montréal, 1375, Avenue Thérèse-Lavoie-Roux, Montréal, QC, H2V 0B3, Canada
[13] School of Astronomy and Space Science, Nanjing University, 163 Xianlin Avenue, Nanjing 210023, People's Republic of China
[14] National Astronomical Observatory of Japan, National Institutes of Natural Sciences, Osawa, Mitaka, Tokyo 181-8588, Japan
[15] Department of Earth Science Education, Seoul National University (SNU), 1 Gwanak-ro, Gwanak-gu, Seoul 08826, Republic of Korea
[16] Department of Earth Science and Astronomy, Graduate School of Arts and Sciences, The University of Tokyo, 3-8-1 Komaba, Meguro, Tokyo 153-8902, Japan
[17] Institute of Astronomy and Department of Physics, National Tsing Hua University, Hsinchu 30013, Taiwan
[18] Academia Sinica Institute of Astronomy and Astrophysics, No.1, Sec. 4., Roosevelt Road, Taipei 10617, Taiwan
[19] SOFIA Science Center, Universities Space Research Association, NASA Ames Research Center, Moffett Field, California 94035, USA
[20] CAS Key Laboratory of FAST, National Astronomical Observatories, Chinese Academy of Sciences, People's Republic of China
[21] National Astronomical Observatories, Chinese Academy of Sciences, A20 Datun Road, Chaoyang District, Beijing 100012, People's Republic of China
[22] Instituto de Astrofísica e Ciências do Espaço, Universidade do Porto, CAUP, Rua das Estrelas, PT4150-762 Porto, Portugal
[23] SKA Organisation, Jodrell Bank, Lower Withington, Macclesfield, SK11 9FT, UK
[24] Jodrell Bank Centre for Astrophysics, School of Physics and Astronomy, University of Manchester, Manchester, M13 9PL, UK
[25] Purple Mountain Observatory and Key Laboratory of Radio Astronomy, Chinese Academy of Sciences, 10 Yuanhua Road, Nanjing 210023, China
[26] Institute of Astronomy, National Central University, Zhongli 32001, Taiwan
[27] Department of Physics and Astronomy, University of Victoria, Victoria, BC V8W 2Y2, Canada
[28] Department of Astronomy and Space Science, Chungnam National University, 99 Daehak-ro, Yuseong-gu, Daejeon 34134, Republic of Korea
[29] School of Physics, Astronomy & Mathematics, University of Hertfordshire, College Lane, Hatfield, Hertfordshire AL10 9AB, UK
[30] NRC Herzberg Astronomy and Astrophysics, 5071 West Saanich Road, Victoria, BC V9E 2E7, Canada
[31] Astrophysics Research Institute, Liverpool John Moores University, IC2, Liverpool Science Park, 146 Brownlow Hill, Liverpool, L3 5RF, UK
[32] Department of Physics and Astronomy, The University of Manitoba, Winnipeg, Manitoba R3T2N2, Canada
[33] Department for Physics, Engineering Physics and Astrophysics, Queen's University, Kingston, ON, K7L 3N6, Canada
[34] National Radio Astronomy Observatory, 520 Edgemont Road, Charlottesville, VA 22903, USA
[35] Jodrell Bank Centre for Astrophysics, School of Physics and Astronomy, University of Manchester, Oxford Road, Manchester, M13 9PL, UK

[36] School of Physics and Astronomy, Cardiff University, The Parade, Cardiff, CF24 3AA, UK
[37] Department of Physics, The Chinese University of Hong Kong, Shatin, N. T., Hong Kong, People's Republic of China
[38] Physics and Astronomy, University of Exeter, Stocker Road, Exeter EX4 4QL, UK
[39] Subaru Telescope, National Astronomical Observatory of Japan, 650 N. A'ohōkū Place, Hilo, HI 96720, USA
[40] Department of Physics and Astronomy, The University of Western Ontario, 1151 Richmond Street, London N6A 3K7, Canada
[41] Department of Physics, Graduate School of Science, Nagoya University, Furo-cho, Chikusa-ku, Nagoya 464-8602, Japan
[42] Department of Environmental Systems Science, Doshisha University, Tatara, Miyakodani 1-3, Kyotanabe, Kyoto 610-0394, Japan
[43] Division of Theoretical Astronomy, National Astronomical Observatory of Japan, Mitaka, Tokyo 181-8588, Japan
[44] Hiroshima Astrophysical Science Center, Hiroshima University, Kagamiyama 1-3-1, Higashi-Hiroshima, Hiroshima 739-8526, Japan
[45] Department of Physics, Hiroshima University, Kagamiyama 1-3-1, Higashi-Hiroshima, Hiroshima 739-8526, Japan
[46] Core Research for Energetic Universe (CORE-U), Hiroshima University, Kagamiyama 1-3-1, Higashi-Hiroshima, Hiroshima 739-8526, Japan
[47] European Southern Observatory, Karl-Schwarzschild-Str. 2, D-85748 Garching, Germany
[48] SOKENDAI (The Graduate University for Advanced Studies), Hayama, Kanagawa 240-0193, Japan
[49] Department of Physics and Astronomy, University College London, WC1E 6BT London, UK
[50] Astrophysics Group, Cavendish Laboratory, J.J. Thomson Avenue, Cambridge CB3 0HE, UK
[51] Kavli Institute for Cosmology, Institute of Astronomy, University of Cambridge, Madingley Road, Cambridge, CB3 0HA, UK
[52] Faculty of Pure and Applied Sciences, University of Tsukuba, 1-1-1 Tennodai, Tsukuba, Ibaraki 305-8577, Japan
[53] OSL, Physics & Astronomy Department, University College London, WC1E 6BT London, UK
[54] Department of Physics, School of Science and Technology, Kwansei Gakuin University, 2-1 Gakuen, Sanda, Hyogo 669-1337, Japan
[55] Nobeyama Radio Observatory, National Astronomical Observatory of Japan, National Institutes of Natural Sciences, Nobeyama, Minamimaki, Minamisaku, Nagano 384-1305, Japan
[56] Astronomical Institute, Graduate School of Science, Tohoku University, Aoba-ku, Sendai, Miyagi 980-8578, Japan
[57] Department of Astronomy, Graduate School of Science, The University of Tokyo, 7-3-1 Hongo, Bunkyo-ku, Tokyo 113-0033, Japan
[58] Department of Physics and Astronomy, McMaster University, Hamilton, ON L8S 4M1, Canada
[59] Department of Physics and Atmospheric Science, Dalhousie University, Halifax B3H 4R2, Canada
[60] Department of Space, Earth & Environment, Chalmers University of Technology, SE-412 96 Gothenburg, Sweden
[61] School of Space Research, Kyung Hee University, 1732 Deogyeong-daero, Giheung-gu, Yongin-si, Gyeonggi-do 17104, Republic of Korea
[62] University of Chinese Academy of Sciences, Beijing 100049, People's Republic of China
[63] NAOC-UKZN Computational Astrophysics Centre, University of KwaZulu-Natal, Durban 4000, South Africa
[64] Xinjiang Astronomical Observatory, Chinese Academy of Sciences, 150 Science 1-Street, Urumqi 830011, Xinjiang, People's Republic of China
[65] Departamento de Astronomía, Universidad de Concepcíon, Av. Esteban Iturra s/n, Distrito Universitario, 160-C, Chile
[66] Department of Astronomy, Yunnan University, Kunming, 650091, People's Republic of China
[67] Key Laboratory of Modern Astronomy and Astrophysics (Nanjing University), Ministry of Education, Nanjing 210023, People's Republic of China
[68] Key Laboratory for Research in Galaxies and Cosmology, Shanghai Astronomical Observatory, Chinese Academy of Sciences, 80 Nandan Road, Shanghai 200030, People's Republic of China
[69] National Astronomical Observatory of Japan, Mitaka, Tokyo 181-8588, Japan
[70] Faculty of Education & Center for Educational Development and Support, Kagawa University, Saiwai-cho 1-1, Takamatsu, Kagawa, 760-8522, Japan
[71] Department of Astronomy, Graduate School of Science, Kyoto University, Sakyo-ku, Kyoto 606-8502, Japan
[72] Department of Physics and Astronomy, Graduate School of Science and Engineering, Kagoshima University, 1-21-35 Korimoto, Kagoshima, Kagoshima 890-0065, Japan
[73] Department of Physics, Faculty of Science and Engineering, Meisei University, 2-1-1 Hodokubo, Hino, Tokyo 1191-8506, Japan
[74] Astrobiology Center, National Institutes of Natural Sciences, 2-21-1 Osawa, Mitaka, Tokyo 81-8588, Japan
[75] Xinjiang Astronomical Observatory, Chinese Academy of Sciences, 830011 Urumqi, People's Republic of China
[76] Physics & Astronomy Dept., University College London, WC1E 6BT London, UK
[77] Purple Mountain Observatory, Chinese Academy of Sciences, 2 West Beijing Road, 210008 Nanjing, People's Republic of China
[78] Laboratoire AIM CEA/DSM-CNRS-Université Paris Diderot, IRFU/Service d'Astrophysique, CEA Saclay, F-91191 Gif-sur-Yvette, France
[79] Jet Propulsion Laboratory, M/S 169-506, 4800 Oak Grove Drive, Pasadena, CA 91109, USA
[80] University of South Wales, Pontypridd, CF37 1DL, UK
[81] Department of Applied Mathematics, University of Leeds, Woodhouse Lane, Leeds LS2 9JT, UK
[82] Univ. Grenoble Alpes, CNRS, IPAG, F-38000 Grenoble, France
[83] School of Physics and Astronomy, University of Leeds, Woodhouse Lane, Leeds LS2 9JT, UK
Received 2020 October 21; revised 2020 December 1; accepted 2020 December 3; published 2021 February 8

Abstract

We report the first high spatial resolution measurement of magnetic fields surrounding LkHα 101, part of the Auriga–California molecular cloud. The observations were taken with the POL-2 polarimeter on the James Clerk Maxwell Telescope within the framework of the B-fields In Star-forming Region Observations (BISTRO) survey. Observed polarization of thermal dust emission at 850 μm is found to be mostly associated with the redshifted gas component of the cloud. The magnetic field displays a relatively complex morphology. Two variants of the Davis–Chandrasekhar–Fermi method, unsharp masking and structure function, are used to calculate the strength of magnetic fields in the plane of the sky, yielding a similar result of $B_{\rm POS} \sim 115$ μG. The mass-to-magnetic-flux ratio in critical value units, $\lambda \sim 0.3$, is the smallest among the values obtained for other regions surveyed by POL-2. This implies that the LkHα 101 region is subcritical, and the magnetic field is strong enough to prevent gravitational collapse. The inferred $\delta B/B_0 \sim 0.3$ implies that the large-scale component of the magnetic field dominates the turbulent one. The variation of the polarization fraction with total emission intensity can be fitted by a power law with an index of $\alpha = 0.82 \pm 0.03$, which lies in the range previously reported for molecular clouds. We find that the polarization fraction decreases rapidly with proximity to the only early B star (LkHα 101) in the region. Magnetic field tangling and the joint effect of grain alignment and rotational disruption by radiative torques can potentially explain such a decreasing trend.

Unified Astronomy Thesaurus concepts: Interstellar magnetic fields (845); Molecular clouds (1072); Star formation (1569)

[84] NAOJ Fellow.

1. Introduction

Several factors are thought to play an important role in the formation and evolution of interstellar clouds and protostars, including magnetic fields (B-fields) and turbulence. However, their precise roles, in particular at different stages of the cloud evolution, are not well understood. Models of cloud and star formation, such as the weak-field and strong-field models (Crutcher 2012), describe the different roles played by magnetic fields and turbulence. More observational constraints are required to test the proposed models and, therefore, to better understand the relative importance of magnetic fields and turbulence.

The alignment of dust grains with the magnetic field induces the polarization of light from background stars (Hall & Mikesell 1949; Hiltner 1949) and of thermal dust emission (Hildebrand 1988). The polarization vectors of background starlight are parallel to the magnetic field while those of thermal dust are perpendicular to the magnetic field. Thus, dust polarization has become a popular technique to measure the projected magnetic field direction and strength (Lazarian 2007; Andersson et al. 2015).

B-fields In Star-forming Region Observations (BISTRO) is a large program of the James Clerk Maxwell Telescope (JCMT) that aims to map the magnetic fields in star-forming regions. BISTRO-1 looks at scales of 1000–5000 au within dense cores and filaments of the star-forming regions of the part of the sky known informally as the "Gould Belt" (Ward-Thompson et al. 2017). It has recently been speculated (Alves et al. 2020) that the Gould Belt is not a single, homogeneous ring, but rather a large-scale "gas wave" in the interstellar medium. Whatever the origin of the structure, it remains convenient to refer to the band of star-forming regions seen across the sky as the "Gould Belt," regardless of the cause of this band. The observations were carried out using the polarimeter, POL-2, placed in front of the JCMT Submillimeter Common User Bolometer Array-2 (SCUBA-2; Holland et al. 2013).

In this work, we study the magnetic fields in the densest region of the Auriga–California molecular cloud (AMC) around LkHα 101 using new data taken by POL-2. The observed region is identical to the one labeled LkHα 101-S (S stands for south) in Figure 1 of Broekhoven-Fiene et al. (2018). Auriga–California is part of the Gould Belt, with a total mass of $\sim 10^5\,M_{\odot}$. It is located at $\sim 466 \pm 23$ pc away from Earth (Zucker et al. 2020), with a spatial extent of 80 pc (Lada et al. 2009). Using data from SCUBA-2 at 450 and 850 μm, Broekhoven-Fiene et al. (2018) found that Auriga–California has 59 candidate protostars, out of which 35 are in the LkHα 101 region. Auriga–California was also observed with Herschel/PACS at 70 and 160 μm, Herschel/SPIRE at 250, 350, and 500 μm and by the Caltech Submillimeter Observatory (CSO) at 1.1 mm (Harvey et al. 2013).

Together with the Orion Molecular Cloud (OMC), Auriga–California is one of two nearby giant molecular clouds in the Gould Belt. Although being similar in size, mass, and distance, Auriga–California is very different from Orion. Additionally, observations by Tahani et al. (2018) show that both Orion A and Auriga–California have the same line-of-sight magnetic field morphology associated with them on large scales. Auriga–California is forming less massive stars and about 20 times fewer stars than the OMC. The OMC has 50 OB stars while Auriga–California has only one early B star, LkHα 101, a member of the embedded cluster in NGC 1579 (Herbig et al. 2004). Using a H_2O maser associated with L1482 where LkHα 101 is located, Omodaka et al. (2020) measured parallax corresponding to the distance to the filament of 532 ± 28 pc. Meanwhile, the distance to the B star LkHα 101 is estimated to be 567 ± 68 pc with Gaia DR2 (Gaia Collaboration 2018). Therefore, measuring magnetic fields in Auriga–California is of particular interest to shed light on what governs the star formation efficiency in molecular clouds. The main purpose of the present BISTRO paper is to use polarization data taken with POL-2 to measure the strength and characterize the morphology of the magnetic field in the region.

The structure of the paper is as follows: in Section 2, we describe the observations; in Section 3, we discuss the extraction of polarization angle dispersion, velocity dispersion, and densities needed for estimating the magnetic field strengths. In Section 4, we present the main results and interpretation of observational data. Our conclusions are presented in Section 5.

2. Observations

2.1. Data Description and Selection

JCMT is a 15 m diameter telescope situated near the summit of Maunakea. It is the largest single-dish telescope working at submillimeter wavelengths between 1.4 and 0.4 mm. The present work studies the polarized emission received from the LkHα 101 region at 850 μm. The beam size at this wavelength is 14.″1. The JCMT detector, SCUBA-2, consists of four arrays of 40×32 bolometers each, covering a solid sky angle of $\sim 45' \times 45'$. The BISTRO program has been allocated two observation campaigns, called BISTRO-1 and BISTRO-2, each having 224 hours to map the regions towards Auriga, IC 5146, Ophiuchus, L1689B, Orion A&B, Perseus B1, NGC 1333, Serpens, Taurus B211/213, L1495, Serpens Aquila, M16, DR15, DR21, NGC 2264, NGC 6334, Mon R2, and Rosette. Recently, a third campaign, BISTRO-3, which focuses on mapping various massive clouds, some nearby prestellar cores, and the Galactic Center clouds, has been approved. General descriptions of the BISTRO survey and the measurement of magnetic fields have been reported for Orion A (Pattle et al. 2017; Ward-Thompson et al. 2017), Ophiuchus A/B/C (Kwon et al. 2018; Soam et al. 2018; Liu et al. 2019; Pattle et al. 2019), IC 5146 (Wang et al. 2019), Perseus B1 (Coudé et al. 2019), M16 (Pattle et al. 2018), and NGC 1333 (Doi et al. 2020).

LkHα 101 was the last region to be observed within the framework of the BISTRO-1 program. The data were taken over nine days between 2017 and 2019 with 21 visits and a total integration time of about 14 hours. The last two observations were made on 2019 January 8. Data were read and reduced using Starlink (Currie et al. 2014). In this analysis, we use gridded data with pixel size of $12'' \times 12''$, similar to the telescope beam. The Stokes parameter Q, U, and I time streams are reduced using pol2map, a POL-2-specific implementation of the iterative map-making procedure makemap (Chapin et al. 2013). The instrumental polarization (IP) is mainly caused by the wind blind; it is corrected for by using the IP model determined from POL-2 measurements with the wind blind in place from observations of Uranus (Friberg et al. 2018). In each pixel, the total intensity, I, the Stokes parameters Q, U, and their uncertainties, δI, δQ, and δU, are provided. The POL-2 data presented in this paper are available at https://doi.org/10.11570/20.0011.

Figure 1 (left) shows the location of the POL-2 observed field in the LkHα 101 area. The 850 μm intensity map, I map,

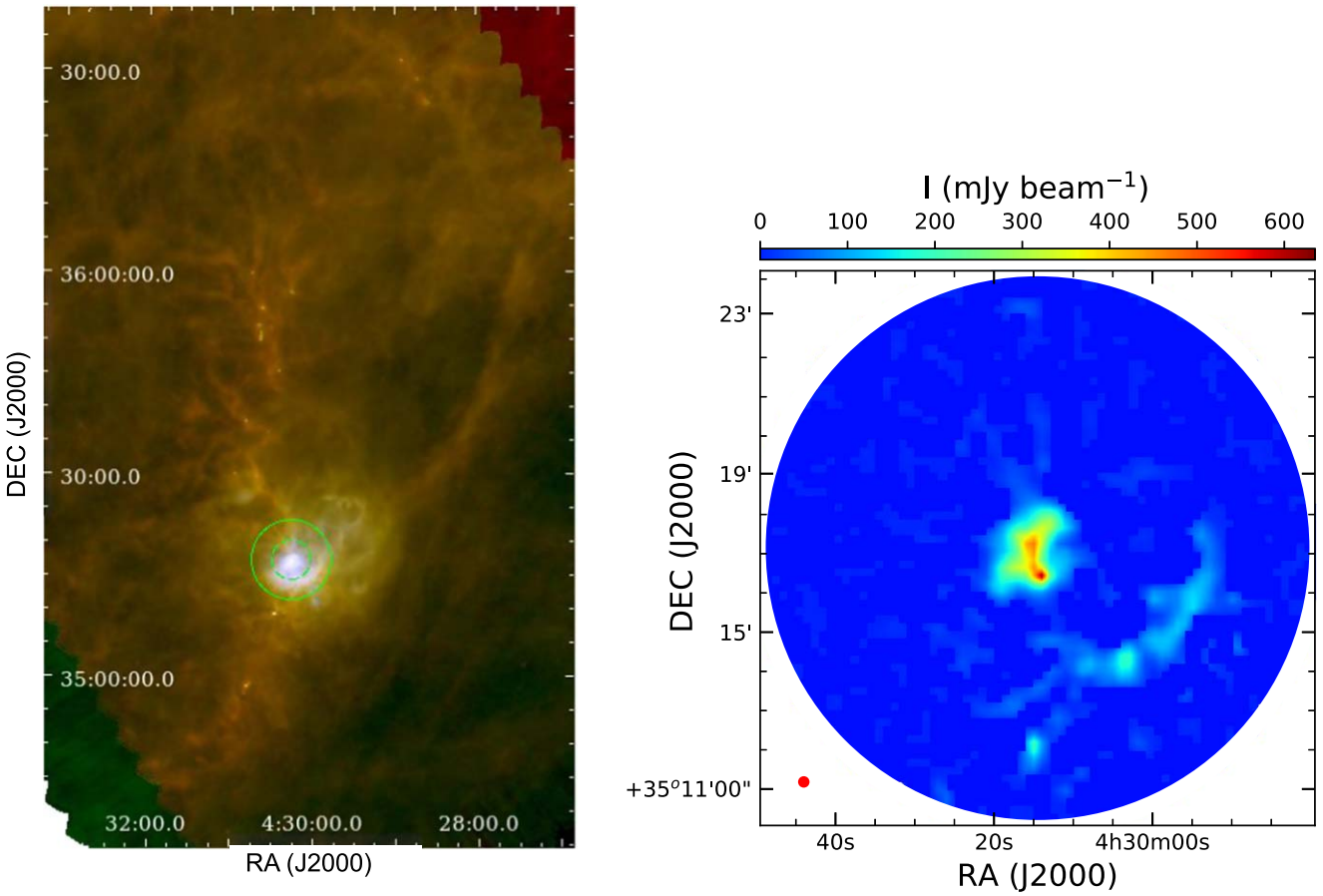

Figure 1. Left: the LkHα 101 field observed by POL-2 overlaid on the Herschel RGB image (R = 250 μm, G = 160 μm, B = 70 μm; Harvey et al. 2013). The green outer circle represents the 6′ radius field of POL-2 and the green inner circle indicates the inner 3′ radius with the best sensitivity. Right: 850 μm intensity map. The red circle at the lower-left corner of the panel shows the JCMT 850 μm beam size of 14″.

is shown in the right panel of the figure. The center of the map is at R. A. = $4^h30^m15^s$, decl.=35°17′05″. Emission is observed to come from a region at the center of the map and a lane of dust in the southwestern direction. It matches the densest area of the region shown in the top-left panel of Figure 2 of Broekhoven-Fiene et al. (2018).

Figure 2 shows the maps of the measured Stokes Q (upper left) and U (upper right) and the distributions of their uncertainties, δQ and δU (lower), which are used to calculate other polarization parameters for further analysis. The distributions of δQ and δU have the same mean and rms values of 1.1 mJy beam^{-1} and 0.5 mJy beam^{-1}, respectively. The mean value of δQ and δU measured in the region is at the level expected for the BISTRO survey (~3 mJy beam^{-1} for the 4″ pixel map).

The debiased polarized intensity, PI, is calculated using the following formula:

$$PI = \sqrt{Q^2 + U^2 - \delta PI^2} \quad (1)$$

(Montier et al. 2015a, 2015b), where the uncertainty on PI is

$$\delta PI = \sqrt{\frac{Q^2\delta Q^2 + U^2\delta U^2}{Q^2 + U^2}}. \quad (2)$$

The polarization angle is defined as

$$\theta = 0.5 \tan^{-1}\left(\frac{U}{Q}\right) \quad (3)$$

and its uncertainty

$$\delta\theta = 0.5 \times \frac{\sqrt{U^2\delta Q^2 + Q^2\delta U^2}}{(Q^2 + U^2)}. \quad (4)$$

We note that the orientation of the magnetic field line is perpendicular to the polarization angle assuming that the polarization of the emission comes from elongated grains that interact with an underlying magnetic field. The angle of the magnetic field line is east of north, ranging from 0° to 180°. Finally, the polarization fraction, P, and its uncertainty, δP, are calculated as

$$P(\%) = 100 \times \frac{PI}{I} \quad (5)$$

and

$$\delta P(\%) = 100 \times \sqrt{\frac{\delta PI^2}{I^2} + \frac{\delta I^2(Q^2 + U^2)}{I^4}}. \quad (6)$$

In an attempt to select measurements to be retained for further analysis, we plot in Figure 3 correlations relating the uncertainties of the measured parameters (no cut has been applied). From the left panel of the figure, it is clear that δI and δPI are strongly correlated. When I is well measured, so is PI; the converse also holds. It is not the case for other parameters in which the correlations are weak (see Figure A1) except for the case of δP versus $\delta\theta$ (Figure 3, right), where we find that most of the good

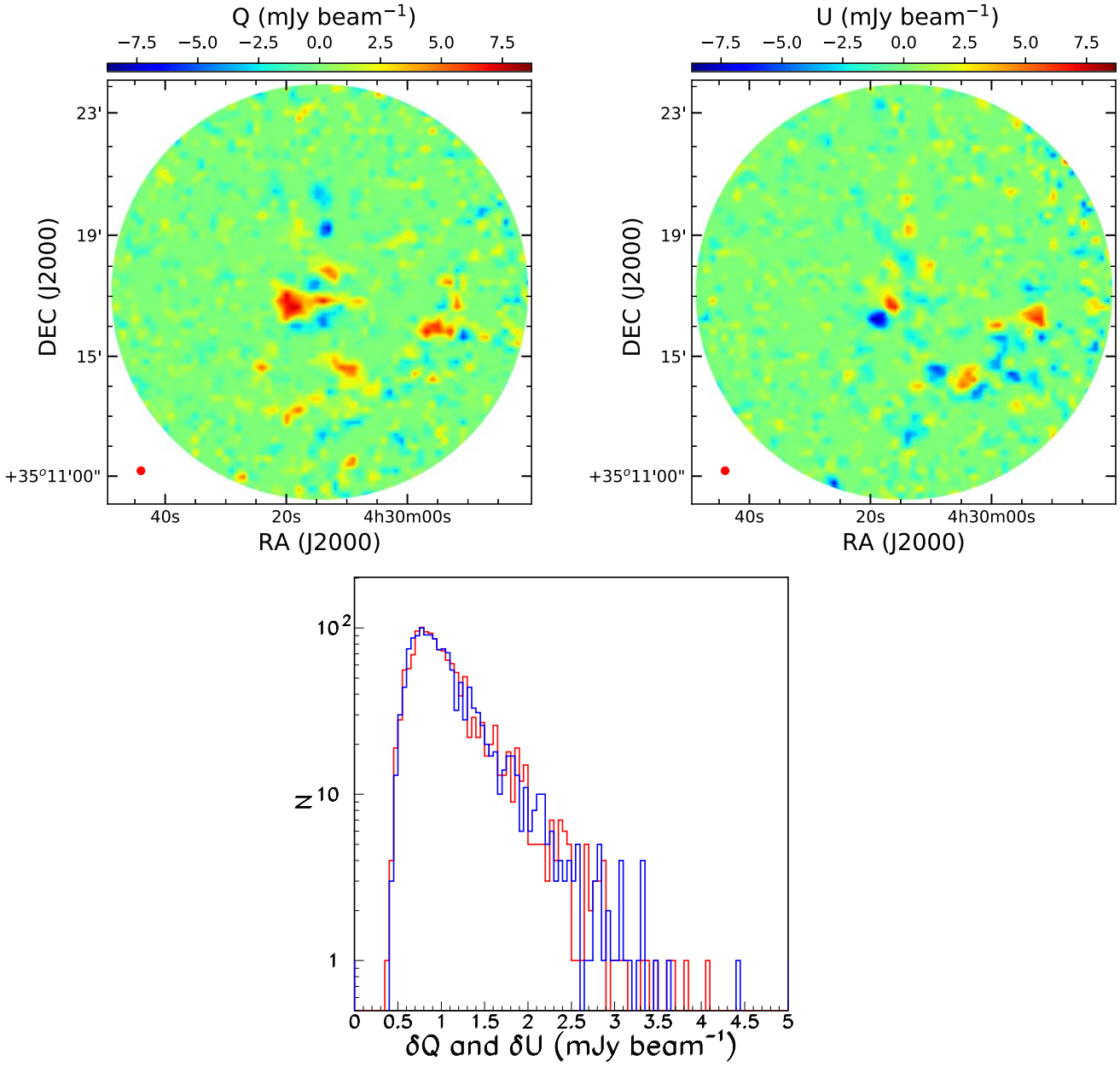

Figure 2. Upper: Q (left) and U (right) maps; the red circles at the lower-left corners indicate the JCMT beam size at 850 μm of 14″. Lower: distributions of δQ (red) and δU (blue).

measurements are confined within a parabola shown as a red solid curve. The equation of the parabola is $\delta P = -0.07\delta\theta^2 + 1.4\delta\theta$. In fact, δP and $\delta\theta$ are related quantities; Serkowski (1962) gives $\delta\theta = 28.65^\circ \delta P/P$. In the following analyses, we use only the data obeying $\delta P < -0.07\delta\theta^2 + 1.4\delta\theta$ (hereafter called the $\delta P{-}\delta\theta$ cut). Because the 850 μm polarized emission from the LkHα 101 region is weak, possibly the weakest in comparison with other regions surveyed by BISTRO, after several attempts, we found that the best compromise between keeping the highest quality data and having good statistics is to use the $\delta P{-}\delta\theta$ cut, which can still ensure the robustness of the results and conclusions of the current studies.

Figure 4 shows the distributions of $I/\delta I$, $PI/\delta PI$, and $P/\delta P$ for the observed region before and after the $\delta P{-}\delta\theta$ cut is applied. These signal-to-noise ratios (S/Ns) measure the quality of the measurements of the corresponding quantities I, PI, and P. Their dimensionless values (mean, rms) are (12.1, 19.8), (2.1, 1.9), and (1.7, 2.0) for $I/\delta I$, $PI/\delta PI$, and $P/\delta P$, respectively. When applying the $\delta P{-}\delta\theta$ cut, these numbers become (38.5, 22.7), (4.0, 2.4), and (3.9, 2.4): the $\delta P{-}\delta\theta$ cut eliminates the parts of the distributions having low S/N. Some more detailed information about the raw data set can be found in the Appendix.

Figure 5 shows the map of the inferred B-fields of the LkHα 101 region keeping only pixels obeying the $\delta P{-}\delta\theta$ cut. The line segments are rotated 90° from the polarization vectors to follow the magnetic field in the plane of the sky. These are called half-vectors because there is an ambiguity in their directions. After application of the $\delta P{-}\delta\theta$ cut, the number of remaining line segments is 419. This map is a direct result of the observations and will be used for further analysis and discussions in the next sections.

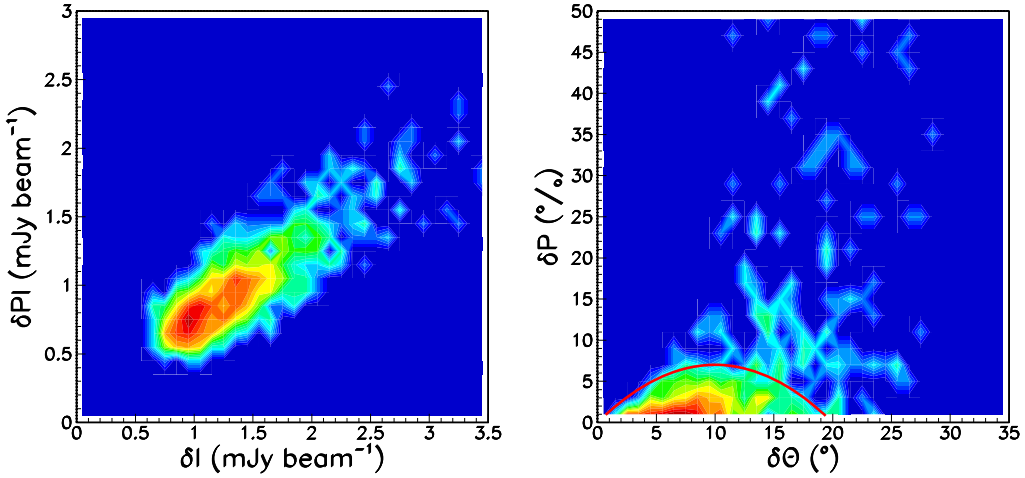

Figure 3. Correlations of measurement uncertainties (the color represents the number of data points in logarithmic scales): δPI vs. δI (left) and δP vs. $\delta\theta$ (right). A strong correlation is found for δPI vs. δI (left panel). Pixels with well-defined polarization fraction ($\delta P < \sim 7\%$) and polarization angles ($\delta\theta < \sim 20^{\circ}$) are encompassed by a parabola (red curve in the right panel).

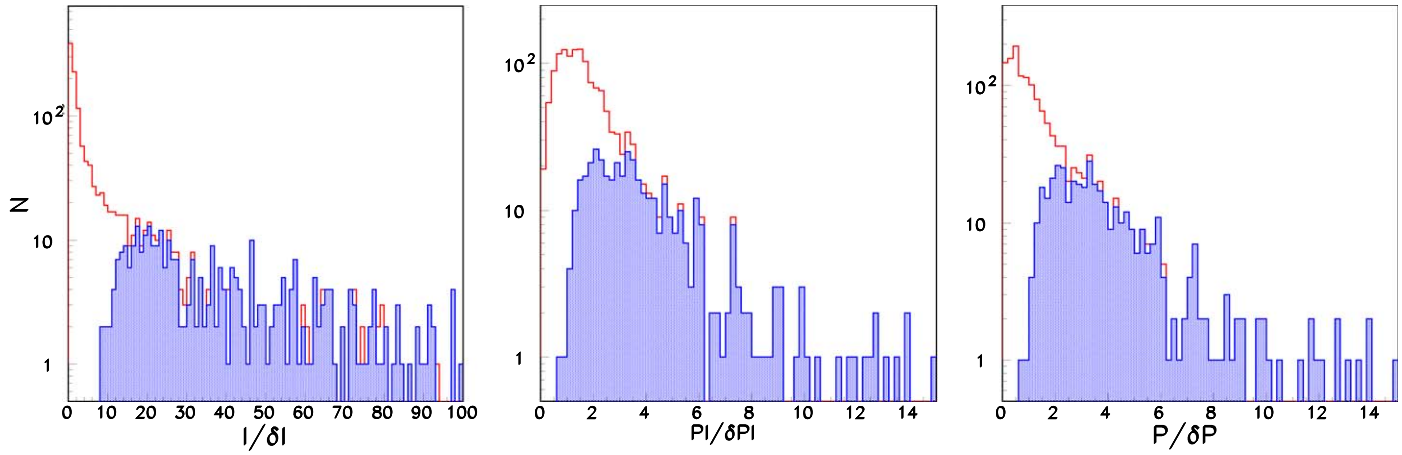

Figure 4. Distributions of $I/\delta I$ (left), $PI/\delta PI$ (center), and $P/\delta P$ (right): all pixels (red histograms) and pixels retained after employing the $\delta P{-}\delta\theta$ cut having high S/N (blue histograms).

3. Polarization Angle Dispersion, Velocity Dispersion, and Densities

3.1. Davis–Chandrasekhar–Fermi Method

It was shown by Davis (1951) and Chandrasekhar & Fermi (1953) that turbulent motions generate irregular magnetic fields. Based on the analysis of the small-scale randomness of the magnetic field lines, assuming that the dispersion in the magnetic field angles is proportional to the Alfvén Mach number, the field strength can be estimated. This is called the Davis–Chandrasekhar–Fermi (DCF) method. A variant of the method has been proposed by Crutcher (2012); it gives an estimate of the magnitude of the magnetic field in the plane of the sky, $B_{\rm POS}$, as

$$B_{\rm POS} = Q\sqrt{4\pi\rho}\,\frac{\sigma_V}{\sigma_\theta} \approx 9.3\sqrt{n({\rm H}_2)}\,\frac{\Delta {\rm V}}{\sigma_\theta} \quad (\mu{\rm G}), \tag{7}$$

where Q is the factor used to correct for the line-of-sight and beam-integration effects (Ostriker et al. 2001), ρ is the gas density, σ_V the one-dimensional nonthermal velocity dispersion in km s^{-1}, $\Delta V = 2.355\sigma_V$, σ_θ is the dispersion of the polarization position angles about a mean B-field in degrees, and $n({\rm H}_2)$ is the number density of molecular hydrogen in units of cm^{-3}.

In the next sections, we evaluate the magnetic field angle dispersion, σ_θ, a measurable of BISTRO, using two different methods.

3.2. Polarization Angle Dispersion: Unsharp Masking Method

To estimate the dispersion of the polarization angle, we first use the "unsharp masking" method which was introduced by Pattle et al. (2017). The principle of the method is to look for the turbulent component of the magnetic field by removing a mean field using a boxcar filter. In practice, this is done by looping over all the pixels of the map, calculating the difference between the original polarization angle map and the intensity-weighted mean map consisting of a 3×3 pixel box centered on the considered pixel. The standard deviation of the distribution of deviation angles, $\Delta\theta = \theta_{\rm meas} - \langle\theta\rangle$, represents the turbulent component of the field and gives the angular dispersion of the region. This process is illustrated in Figure 6.

We apply this method to calculate the angle dispersion for the central region and the southwestern dust lane (hereafter called CR for the central region and DL for the dust lane). The CR is defined as having $R < 120''$ from the map center, and the DL is the region

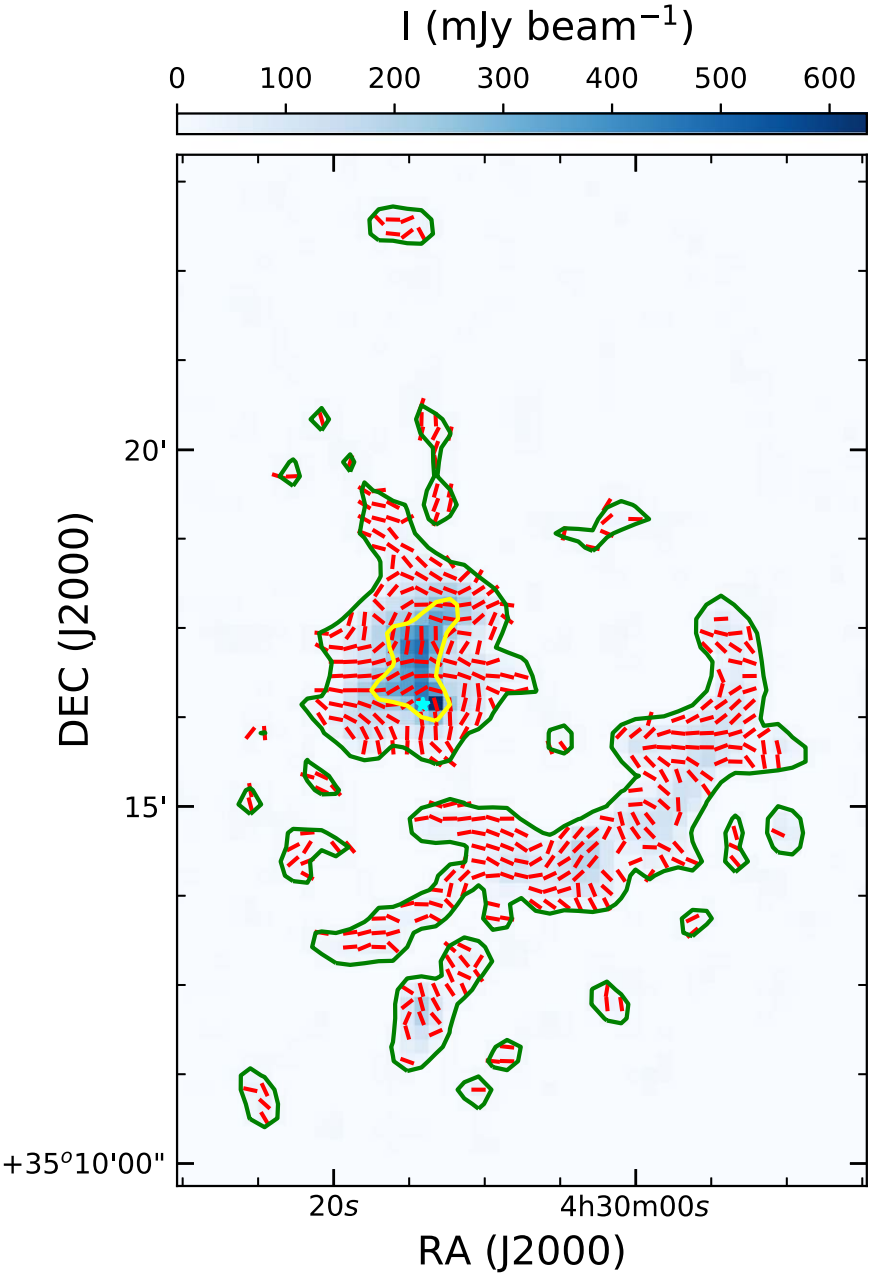

Figure 5. Map of the inferred magnetic field orientation (line segments) overlaid on the 850 μm emission intensity map (color scale). The green contours correspond to 15 mJy beam^{-1} and the yellow contour to 250 mJy beam^{-1}. The line segments shown are those remaining after the $\delta P-\delta\theta$ cut. The location of the B star LkHα 101 is at the cyan star marker at R. A. $= 4^h30^m14\overset{s}{.}4$, decl. $= 35°16'24''$.

surrounded by an ellipse having a center at RA $\sim 4^h30^m4\overset{s}{.}7$ and DEC $\sim +35°14'47\overset{''}{.}8$, major $\times$ minor axes of $300'' \times 108''$, and a position angle of 135° (see Figure 1, right, and the white curves in Figure 9). The angle dispersion obtained by requiring $|\Delta\theta| < 90°$ (to avoid the effect of the $\pm 180°$ ambiguity of the magnetic field lines) are $\sigma_\theta = 17.2° \pm 0.4°$ and $17\overset{°}{.}1 \pm 0\overset{°}{.}5$ for the CR and the DL, respectively. To understand how the dispersion depends on the measurement uncertainties, we list in Table 1 the polarization angle dispersion as a function of cuts applied on δI, in addition to the $\delta P-\delta\theta$ cut. Exploring the δI dependence is sufficient because δI and δPI are strongly correlated (Figure 3 left). We note that δI ranges from ~0.6 to ~5.0 mJy beam^{-1} (Figure A2).

We see from Table 1 that the angle dispersion is robust while applying an additional cut requiring higher S/N measurements of the total and polarized intensities. This is an indication that $\delta P-\delta\theta$ is a robust cut. Only in the case of the most rigorous cut requiring $\delta I < 1$ mJy beam^{-1} for the DL does the number of remaining half-vectors drastically decrease from ~190 to 12 with the angle dispersion decreasing from $\sigma_\theta \sim 17°$ to $5\overset{°}{.}8$.

The uncertainties of the polarization angle dispersion are also studied following the procedure of this same method (Pattle et al. 2017). Figure 7 displays the dependence of the angle dispersion on the maximum allowed uncertainties, $\delta\theta_{\rm max}$, for each boxcar filter. In practice, this means that the angle dispersion of the map is calculated by requiring that the maximum uncertainty of all the pixels in each 3×3 boxcar filter be smaller than $\delta\theta_{\rm max}$. The polarization angle dispersion is expected to increase with the maximum allowed uncertainty of the boxcar filters. Indeed, as can

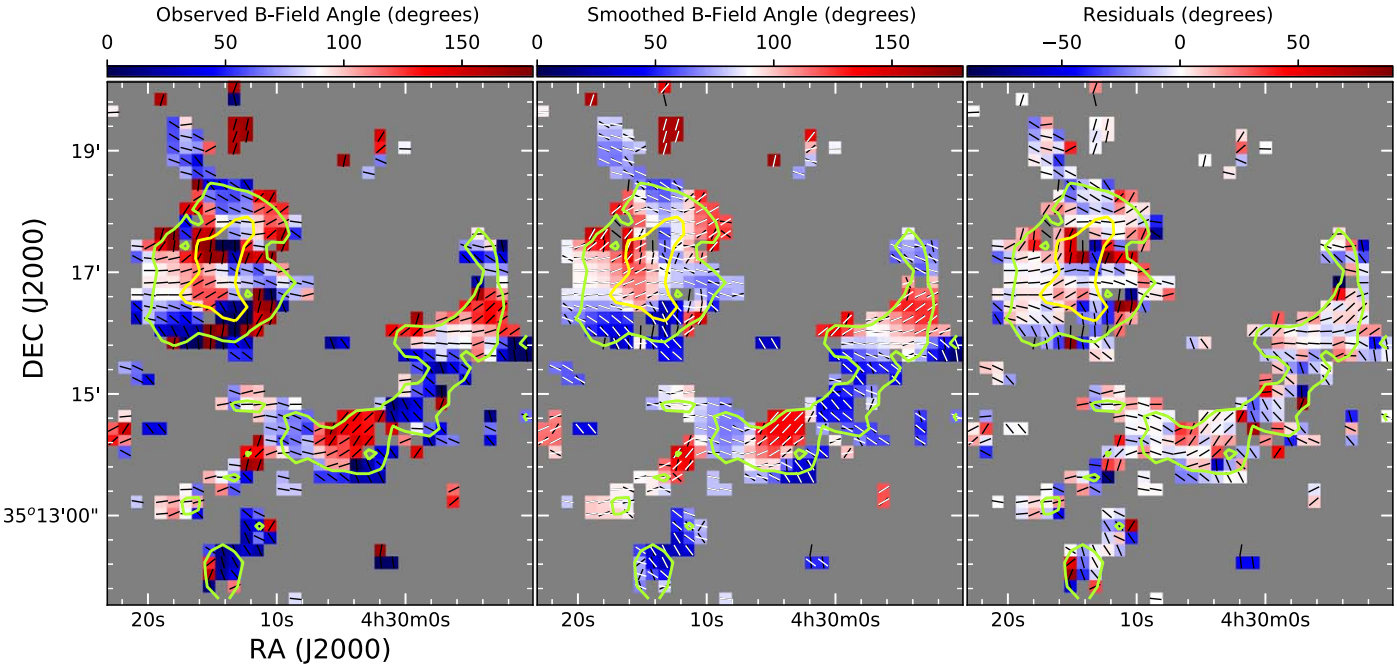

Figure 6. B-field angle maps: original (left), smoothed (center), and residual (right). The green contours correspond to 50 mJy beam^{-1} and the yellow contours to 250 mJy beam^{-1}. In all panels, the orientation of the measured magnetic field half-vectors is plotted in black. In addition, in the central panel, the orientation of the smoothed half-vectors is shown in white.

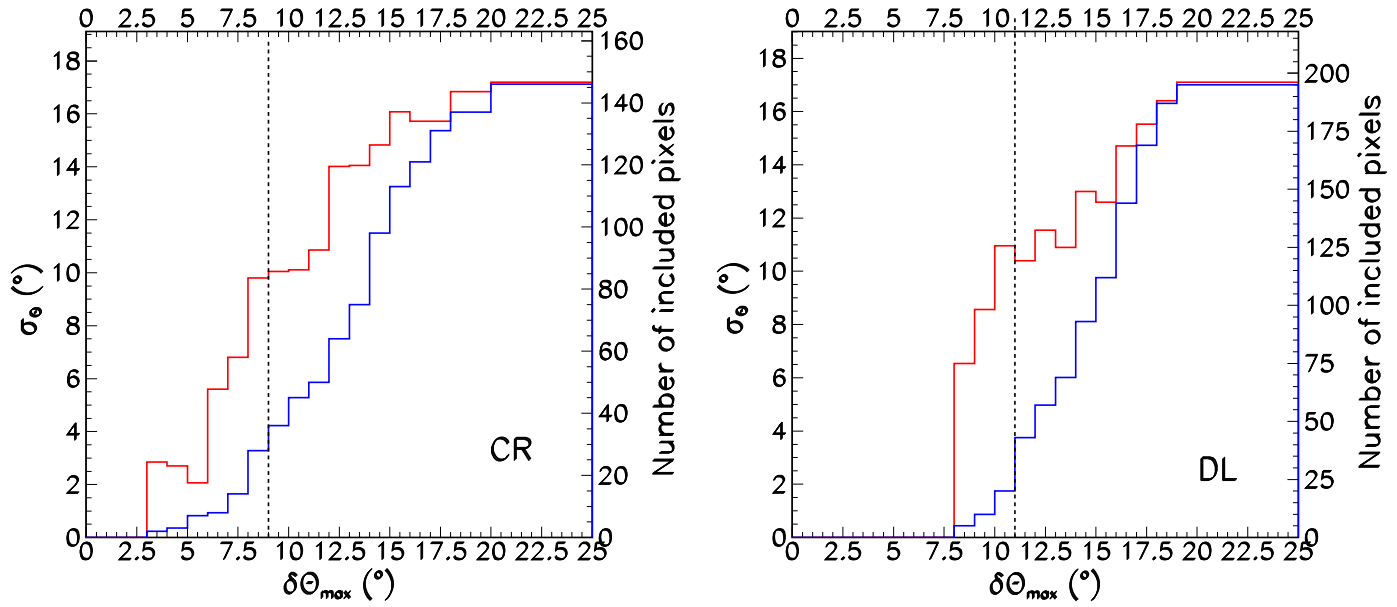

Figure 7. Dependence of the polarization angle dispersion (red) and number of included pixels (blue) on the maximum allowed uncertainties $\delta\theta_{\max}$ for the central region (left) and the dust lane (right). Black dashed lines show the lower limit of $\delta\theta_{\max}$ over which the average angle dispersion is calculated.

Table 1
Dependence of Angle Dispersion and Number of Remaining Half-vectors, $N_{\rm rm}$, on δI Cuts

	δI (mJy beam^{-1})<	1.0	1.5	2.0	2.5	3.0	4.0
Central Region	$\sigma_\theta(^\circ)/N_{\rm rm}$	16.0/94	17.1/135	17.5/141	17.6/142	17.3/144	17.2/146
Dust Lane	$\sigma_\theta(^\circ)/N_{\rm rm}$	5.8/12	17.1/192	17.1/195	17.1/195	17.1/195	17.1/195

be seen from Figure 7 (left for the CR and right for the DL), the angle dispersion increases as $\delta\theta_{\max}$ increases. As was done by Soam et al. (2018) and Liu et al. (2019), from the angle dispersion for different $\delta\theta_{\max}$ (Figure 7), we calculate the mean angle dispersion ± uncertainties of $\sigma_\theta = 14.^\circ9 \pm 2.^\circ7$ and $14.^\circ7 \pm 2.^\circ6$ for the CR and the DL, respectively. These values are kept as the final polarization angle dispersion for further analysis. We note that the results are obtained excluding a first few bins of $\delta\theta_{\max}$, where

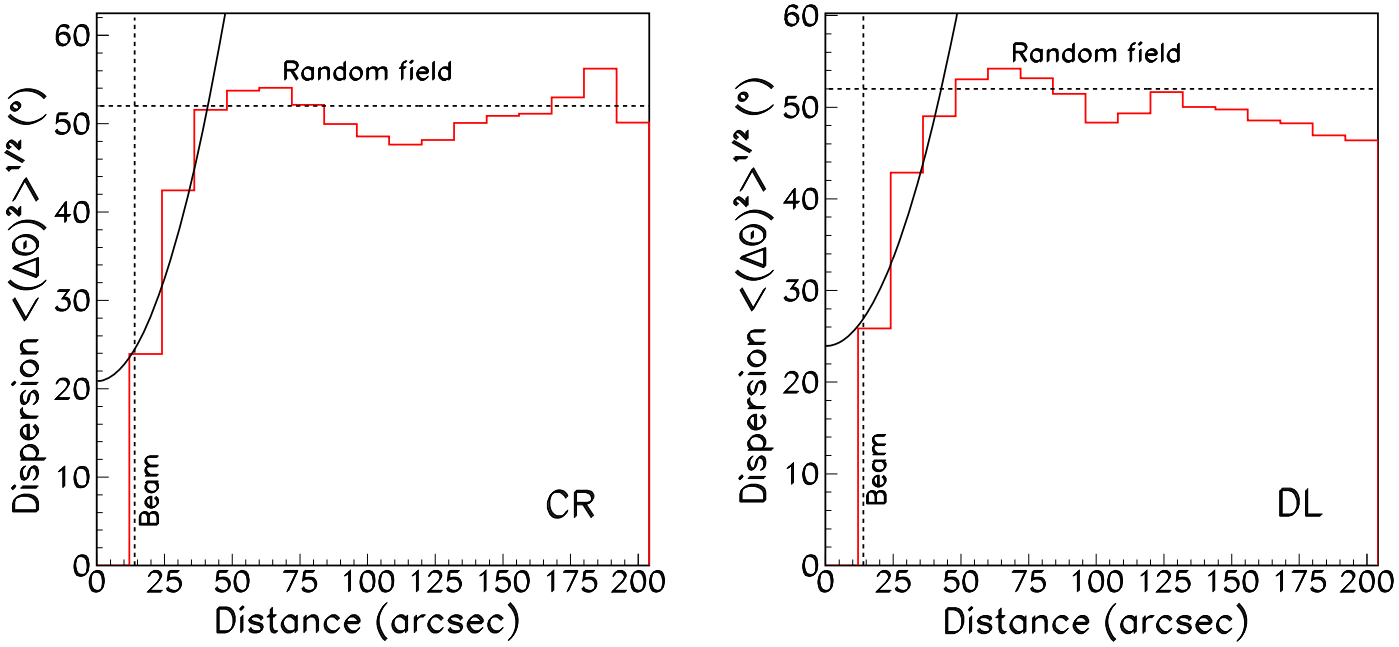

Figure 8. The structure functions calculated for the central region (left) and for the dust lane (right). The horizontal dashed lines are the expected value for random fields. The solid black curves are the results of fits to Equation (9) for the estimation of the polarization angle dispersion of the regions. The vertical dashed lines are at distances equal to the beam size of the JCMT telescope.

the numbers of included pixels are smaller than 20 and with the application of the $\delta P - \delta\theta$ cut.

3.3. Polarization Angle Dispersion: Structure Function

Another method to estimate the dispersion of polarization position angles makes use of the so-called structure function (Hildebrand et al. 2009), which is defined as follows. We consider pairs of pixels, at locations $\boldsymbol{x}$ and $\boldsymbol{x} + \boldsymbol{l}$, each associated with a polarization position angle θ. For a given pixel separation l, the structure function is defined as the mean square angle between the polarization half-vectors of the pair:

$$\langle \Delta\theta^2(l) \rangle = \frac{1}{N(l)} \sum_{i=1}^{N(l)} [\theta(\boldsymbol{x}) - \theta(\boldsymbol{x} + \boldsymbol{l})]^2, \quad (8)$$

where $N(l)$ is the number of such pairs. We assume that the magnetic field $\boldsymbol{B}$ can be approximated by the sum of a large-scale structured field of mean amplitude B_0 and a turbulent component δB; we also assume that the correlation length of the turbulent component is much smaller than the distance over which $\boldsymbol{B}$ varies significantly. For small separations l, we can write

$$\langle \Delta\theta^2(l) \rangle = b^2 + m^2 l^2 + \sigma_M^2(l), \quad (9)$$

where b is the rms contribution of the turbulent component and m measures the contribution of the gradient of $\boldsymbol{B}$; in addition, the contribution of the measurement uncertainties, $\sigma_M(l)$, is included. All of these contributions add in quadrature. Ignoring the contribution of the large-scale structured field in Equation (9) and from the definition of the polarization angle dispersion, σ_θ, we have $\sigma_\theta^2 = b^2/2$.

Hildebrand et al. (2009) expressed the ratio of the turbulent field, δB, to the large-scale underlying field (i.e., mean field), B_0, as

$$\frac{\delta B}{B_0} = \frac{b}{\sqrt{2 - b^2}}, \quad (10)$$

where $b = \sqrt{2}\sigma_\theta$. We note that Equations (9) and (10) hold only if the correlation length of the turbulent component satisfies $\delta < l$ (Hildebrand et al. 2009).

We calculate the structure functions for both the CR and the DL; the result is displayed in Figure 8. At large distances, the structure functions tend to the random field value of $\sim 52°$ (Serkowski 1962). A fit to Equation (9) for short distances, $12'' < l < 36''$, gives $b = 20.^\circ9 \pm 6.^\circ8$ and $23.^\circ9 \pm 7.^\circ1$, namely $\sigma_\theta = 14.^\circ8 \pm 4.^\circ8$ and $16.^\circ9 \pm 5.^\circ0$ for the CR and the DL, respectively. When applying additional cuts on δI, $\delta I < 1$ ($\delta I < 1.5$) mJy beam^{-1}, we obtain values of $\sigma_\theta = 14.^\circ3 \pm 6.^\circ1$ ($14.^\circ5 \pm 4.^\circ9$) for the CR. For the DL, this cannot be done with the 1 mJy beam^{-1} cut because too few half-vectors are retained. With the 1.5 mJy beam^{-1} cut, we obtain $\sigma_\theta = 14.^\circ6 \pm 3.^\circ1$. All of the angle dispersions obtained when applying additional δI cuts are in agreement within one standard deviation with the values obtained when applying the $\delta P - \delta\theta$ cut only. This once again confirms that the choice of the $\delta P - \delta\theta$ cut is robust.

3.4. Column and Number Densities

The dust column density of the Auriga–California molecular cloud has been constructed by Harvey et al. (2013) using four Herschel wavebands at 160, 250, 350, and 500 μm. Using the KOSMA 3 m telescope to detect the CO($J = 2-1$) and ($J = 3-2$) line emissions, Li et al. (2014) studied the morphology of the L1482 molecular filament of the Auriga–California molecular cloud, of which our studied region is part. The column and number densities of 23 identified clumps along L1482 were measured. Our CR, which fits in a circle of 120″ radius, encloses their Clump 10 (an ellipse of 228″ × 110″ major × minor axes); the DL, extending over 600″ × 216″, overlaps with their Clump

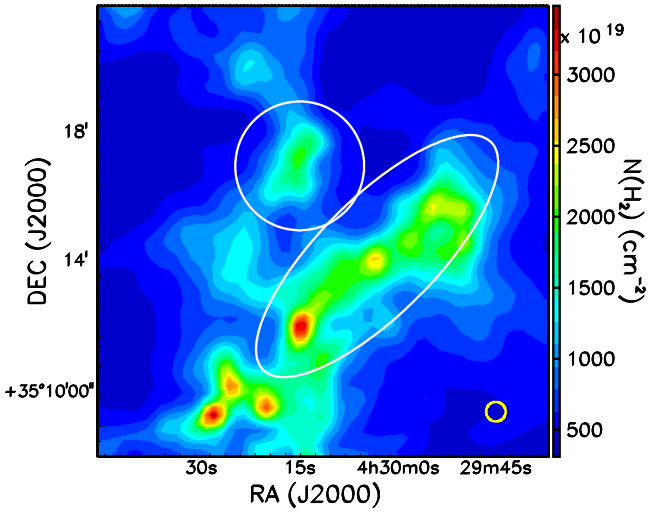

Figure 9. Positions of the central region (white circle) and the dust lane (white ellipse) superposed on the Herschel column density map (Harvey et al. 2013). The Herschel beam size (36.″6) is shown in the lower-right corner of the map.

12 (an ellipse of $195'' \times 68''$ major × minor axes), but is significantly larger. We use the column density map (Figure 9) from Harvey et al. (2013) to calculate the average column densities and number density; we find $N(H_2) = (0.96 \pm 0.39) \times 10^{22}$ cm^{-2} and $n(H_2) = 1.22 \times 10^4$ cm^{-3} over the CR, and $N(H_2) = (1.44 \pm 0.53) \times 10^{22}$ cm^{-2} and $n(H_2) = 1.25 \times 10^4$ cm^{-3} over the DL. The number densities are calculated following the same strategy used by Li et al. (2014) in their Section 3.3.2. The masses of the CR and the DL are calculated using $M = \beta m_{H_2} N_{\mathrm{total},H_2} (D\Delta)^2$, where $\beta = 1.39$ is a factor that takes into account the contribution of He in addition to H_2 to the total mass, m_{H_2} is the mass of a hydrogen molecule, N_{total,H_2} is the total column density, and $\Delta = 14''$ is the pixel size of Herschel data. For consistency, as was done by Harvey et al. (2013), we use the same distance to the LkHα 101 region of $D = 450$ pc to calculate the column densities. The radius of the CR is $120''$, and the radius of the DL is assumed to be $R = \sqrt{(ab)/2}$, where a and b are the major and minor axes of the DL ellipse. Then, the number density of hydrogen molecules is obtained using $n_{H2} = 3M/(4\pi R^3 m_{H_2})$. The relative uncertainties in the number densities are taken to be equal to those of the column densities (42% and 37% for the CR and the DL, respectively).

3.5. Velocity Dispersion

The nonthermal velocity dispersion along the line of sight has been measured by the Purple Mountain Observatory (PMO) 13.7 m radio telescope using the ^{13}CO(1−0) transition (Li et al. 2014). The results are $\sigma_V = 0.52$ km s^{-1} (meaning $\Delta V = 2.355\sigma_V = 1.22$ km s^{-1}) for Clump 10 and $\sigma_V = 0.64$ km s^{-1} (meaning $\Delta V = 2.355\sigma_V = 1.52$ km s^{-1}) for Clump 12.

We also analyzed archival CO(3−2) JCMT/HARP[85] data (Buckle et al. 2009) in order to evaluate the velocity dispersion. Figure 10 (left) displays the velocity-integrated intensity map, and Figure 10 (right) displays the intensity-weighted mean Doppler velocity of the region observed by HARP. We note that when we superimpose the intensity map of the 850 μm emission collected by POL-2 (the blue contours in Figure 10 right) on the mean velocity map, we find that the location of the emission matches very well that of the redshifted arc of the cloud. It suggests a cloud emitting polarized light and moving away from us over a blueshifted background (Figure 10 right). A small clump in the northern part of the map is seen to account for most of the blueshifted emission beyond −2 km s^{-1}; its spectrum is shown in the right panel of Figure 11.

The left panels of Figure 11 show the integrated spectra for the CR (left) and the DL (center); they display a two-component structure. The fits of these spectra to two Gaussians give standard deviations of the blue- and redshifted components $(\sigma_B, \sigma_R) = (0.90 \pm 0.02,\ 0.56 \pm 0.01)$ km s^{-1} and $(0.60 \pm 0.03,\ 0.79 \pm 0.02)$ km s^{-1} with mean values of $(-1.25,\ 0.89)$ km s^{-1} and $(-1.08,\ 0.57)$ km s^{-1} for the CR and the DL, respectively. The average temperatures are 29.7 K for the CR and 20.8 K for the DL (Harvey et al. 2013). The corresponding velocity dispersion caused by thermal turbulence are only at per mil level and therefore negligible: the nonthermal FWHM line widths are equal to $(\Delta V_B, \Delta V_R) = (2.12 \pm 0.05,\ 1.32 \pm 0.02)$ km s^{-1} and $(1.41 \pm 0.07,\ 1.86 \pm 0.05)$ km s^{-1} for the CR and the DL, respectively. Because the redshifted parts of the cloud trace well the 850 μm polarized emission from the region, we use their velocity dispersion to calculate the B-field strength in the next section. However, we conservatively use uncertainties on velocity dispersion estimated from the combination of the three independent measurements added in quadrature: ^{13}CO(1−0) emission (Li et al. 2014), HARP blueshifted, and HARP redshifted spectra instead of using only the uncertainties from the fits to the HARP redshifted spectra. The final velocity dispersions retained for further analysis are 1.32 ± 0.40 km s^{-1} and 1.86 ± 0.19 km s^{-1} for the CR and DL, respectively. Though the velocity dispersion obtained from CO(3−2) (redshifted part) and from ^{13}CO(1−0) agree within ∼20%, which supports the use of the CO(3−2) line emission for calculating the gas velocity dispersion, we note that the CO(3−2) line available to us may not be optically thin. Therefore, the results regarding the magnetic field strength in the current paper are obtained under the assumption that the CO(3−2) line traces the observed dust volume.

4. Results and Discussions

4.1. Magnetic Field Morphology

The B-fields are measured over a region of ∼1.6 pc at a spatial resolution of ∼0.03 pc. With the irregular mass distribution and the presence of several protostar candidates and an early B star in the region, the magnetic field morphology of the observed region is expected to be complex. In fact, it is the case of the B-field patterns at the CR of the map, the highest emission region, which shows a drastic change of the plane-of-the-sky field directions (see Figures 5 and 13). The field lines are perpendicular to each other, running north–south and east–west. This is an indication of the existence of important field turbulence or of the magnetic field tangling in the dense region. The measured polarization angle dispersion of the order of $\sigma_\theta \sim 15°$ also supports the existence of the field turbulence. However, it is identified from the measurement of the ratio of the turbulent field to the large-scale underlying field that the B-fields of the whole LkHα 101 region is still generally dominant over the turbulence (see Section 4.3). Going farther away from the center of the map where the density is lower, the B-fields tend to follow the periphery of the matter distribution. However, for the outermost parts, in particular, where

[85] Heterodyne Array Receiver Program, a single sideband array receiver with 16 mixers of the JCMT. HARP can be tuned between 325 and 375 GHz and has an instantaneous bandwidth of ∼2 GHz.

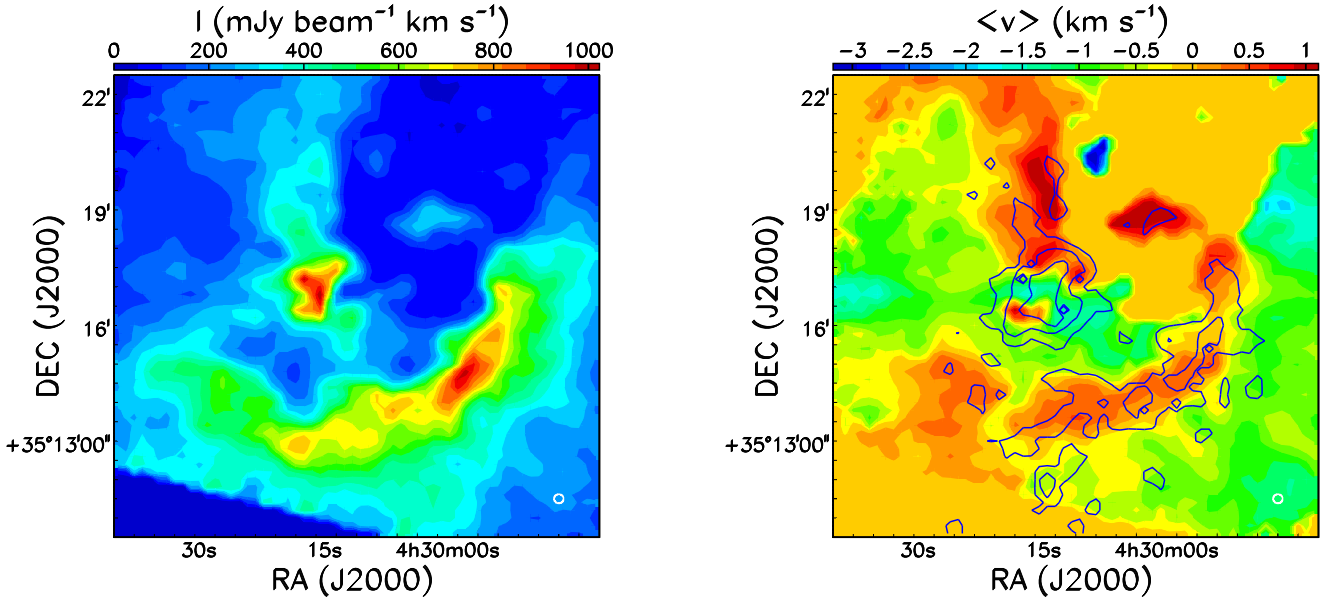

Figure 10. HARP data. Left: CO(3−2) intensity map integrated over ±5.5 km s^{-1}; right: map of the intensity-weighted mean Doppler velocity relative to the mean $v_{\rm LSR}$ of the cloud. The blue contours are the intensity map at 15, 100, and 250 mJy beam^{-1} levels of the 850 μm POL-2 polarized emission (the same as that of Figure 1, right). The HARP beam size (14″) is shown in the lower-right corner of the map.

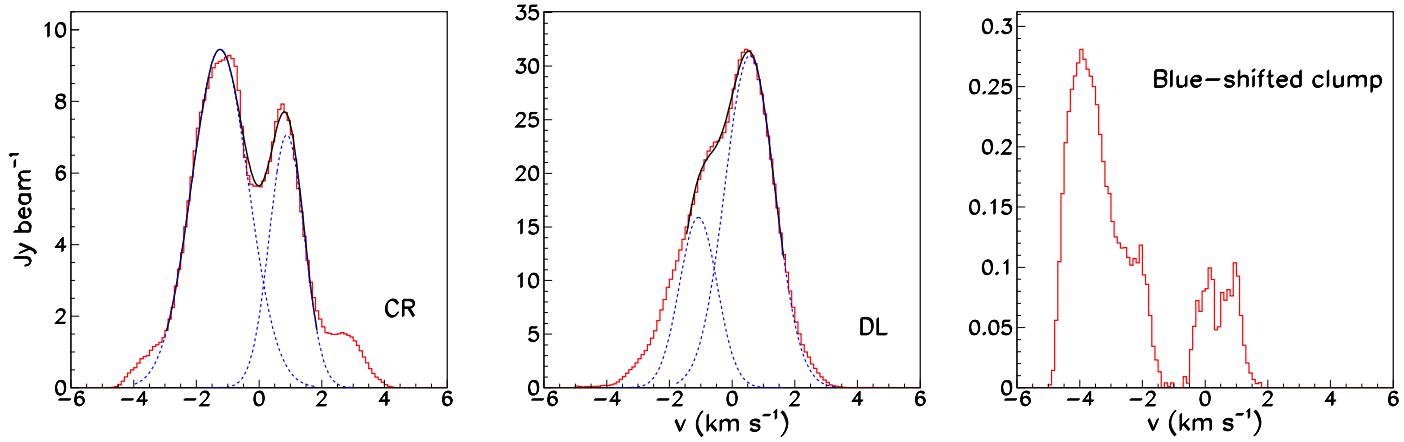

Figure 11. HARP CO(3−2) integrated spectra. Left: central region; center: dust lane. Right: blueshifted clump at RA ∼ $4^{h}30^{m}07^{s}$ and decl.∼+35°13′20.″5. The blue dashed curves are the Gaussian components shown separately. The black curves are the results of the two-Gaussian fits (see text in Section 3.5).

the contour level (green curve in Figure 13) is highly curved, the B-fields are perpendicular to the curve.

In the DL, the main orientation of the B-fields has the tendency to follow the filamentary structure (northwest–southeast) of the DL.

A similar tendency of the field running along the filamentary structure is also found in the low-density clumps enclosed by the green contours in Figure 13 scattered around the CR and the DL. This trend is better seen with the elongated clumps.

Prestellar cores, protostars, and then low-mass stars are believed to form in filaments (André et al. 2014). This paradigm is supported by simulations (e.g., Inoue & Inutsuka 2012; Soler et al. 2013). B-fields help funnel matter onto the filaments. Because the DL is a subcritical filament (see Section 4.3), the overall magnetic field direction parallel to its structure is in agreement with the popular picture of the B-field evolution in star-forming regions. Indeed, at large scale, B-fields are typically perpendicular to the main structure of filaments (e.g., Matthews et al. 2014; Planck Collaboration et al. 2015). At the scale of the core and filament size, it is found roughly that magnetic field runs perpendicular to a filament when the filament is gravitationally supercritical, but parallel when it is subcritical (Palmeirim et al. 2013; Ward-Thompson et al. 2017). However, we note that criticality is not the only parameter to decide the configurations of field versus structure. Planck and BLASTPol[86] data show a parallel-to-perpendicular transition at visual extinction $A_V \sim 3$ mag (Planck Collaboration et al. 2016; Soler et al. 2017). In addition, using SOFIA data in Serpens South, Pillai et al. (2020) found another transition from perpendicular back to parallel at $A_V \gtrsim 21$ mag. Our DL has an average column density of 1.44×10^{22} cm^{-2} (Table 2), which corresponds to $A_V \sim 15.3$ mag. The visual extinction is obtained using the standard conversion factor between column densities and visual extinction $N(H_2) = 9.4 \times 10^{20}$ cm^{-2} A_V mag (Bohlin et al. 1978). Comparing with what is found in Serpens South, the DL lies in the region where the field is perpendicular to the filament (see Figure 3 of Pillai et al. 2020) and close to the region where

[86] A balloon-borne polarimeter.

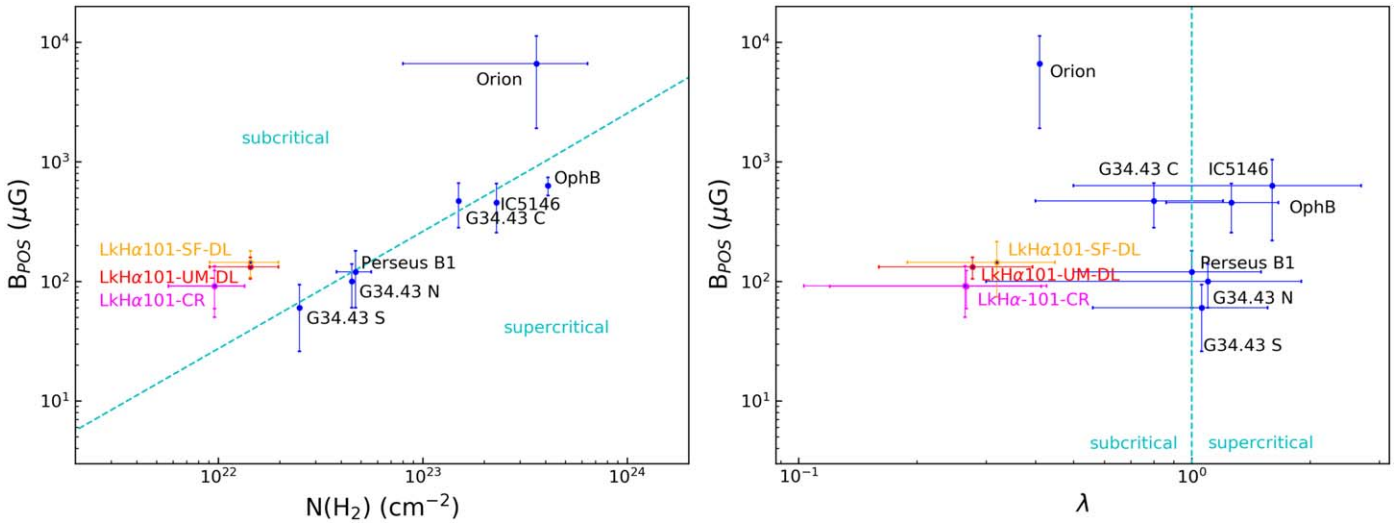

Figure 12. (Left) Dependence of $B_{\rm POS}$ on column density, $N(H_2)$, and (right) mass-to-magnetic-flux ratio, λ. Red and yellow are for the dust lane and for unsharp masking (UM) and structure-function (SF) methods, respectively. Purple is for the central region. The dashed lines separate the super- and subcritical conditions (the one in the left panel is obtained from Equation (12)).

Table 2
Summary of Physical Parameters Estimated for the Central Region and the Dust Lane

		Central Region	Dust Lane
Herschel	Number density, $n(H_2)$ (cm^{-3})	$(1.22 \pm 0.50) \times 10^4$	$(1.25 \pm 0.46) \times 10^4$
	Column density, $N(H_2)$ (cm^{-2})	$(0.96 \pm 0.39) \times 10^{22}$	$(1.44 \pm 0.53) \times 10^{22}$
HARP	Dispersion velocity, ΔV (km s^{-1})	1.32 ± 0.40	1.86 ± 0.19
Unsharp Masking	Polarization angle dispersion, σ_θ (°)	14.9 ± 2.7	14.7 ± 2.6
	$B_{\rm POS}$ (μG)	91 ± 32	132 ± 27
	$\delta B/B_0$	0.269	0.265
	Mass-to-flux ratio, λ	0.27 ± 0.15	0.28 ± 0.12
Structure Function	Polarization angle dispersion, σ_θ (°)	14.8 ± 4.8	16.9 ± 5.0
	$B_{\rm POS}$ (μG)	92 ± 42	144 ± 36
	$\delta B/B_0$	0.267	0.309
	Mass-to-flux ratio, λ	0.27 ± 0.16	0.32 ± 0.15

the median relative orientation of the field and filament crosses 45°. This suggests that the perpendicular-to-parallel transition may vary depending not only on visual extinction but also on other parameters of a cloud. The CR is an example of this. It is also subcritical but the fields are complex with the presence of protostar candidates and an early B star. More statistics will help to settle this issue.

4.2. Magnetic Field Strength

For the DCF method to be applicable, Ostriker et al. (2001) suggested that the polarization angle dispersion should be smaller than ∼25°, which is the case of the present data set. Using the H_2 number densities and the nonthermal velocity dispersion along the line of sight given in Sections 3.4 and 3.5, Equation (7) gives the magnitude of the magnetic field in the plane of the sky, $B_{\rm POS}$. The uncertainties of $B_{\rm POS}$ are propagated using the following relation:

$$\frac{\delta B_{\rm POS}}{B_{\rm POS}} = \sqrt{\left(\frac{1}{2}\frac{\delta n(\mathrm{H_2})}{n(\mathrm{H_2})}\right)^2 + \left(\frac{\delta \Delta V}{\Delta V}\right)^2 + \left(\frac{\delta \sigma_\theta}{\sigma_\theta}\right)^2}, \quad (11)$$

where $\delta n(H_2)$, $\delta \Delta V$, and $\delta \sigma_\theta$ are the uncertainties of $n(H_2)$, ΔV, and σ_θ, respectively.

The magnetic field strengths obtained from two methods are listed in Table 2 for the CR and the DL. As shown, the two methods yield a similar magnetic field strength of $B_{\rm POS} \sim 91\ \mu$G for the CR and $B_{\rm POS} \sim 138\ \mu$G for the DL.

It is very interesting to note that the mean measured field strength of ∼115 μG is very close to the value of 100 μG adopted by Zhang et al. (2020) to explain the observed fragmentation length scale (core spacing) of star-forming filaments in the X-shape nebula of the California molecular cloud.

4.3. Mass-to-flux Ratio

The relative importance of gravity to magnetic fields is usually described by the mass-to-flux ratio, M/Φ. In the units of the critical value, the mass-to-flux ratio is given by the formula from Crutcher (2004),

$$\lambda = \frac{(M/\Phi)_{\rm observed}}{(M/\Phi)_{\rm critical}} = 7.6 \times 10^{-21} \frac{N(\mathrm{H_2})}{B_{\rm POS}}, \quad (12)$$

where $(M/\Phi)_{\rm critical} = 1/(2\pi\sqrt{G})$, G is the gravitational constant, $N(H_2)$ is the gas column density measured in cm^{-2},

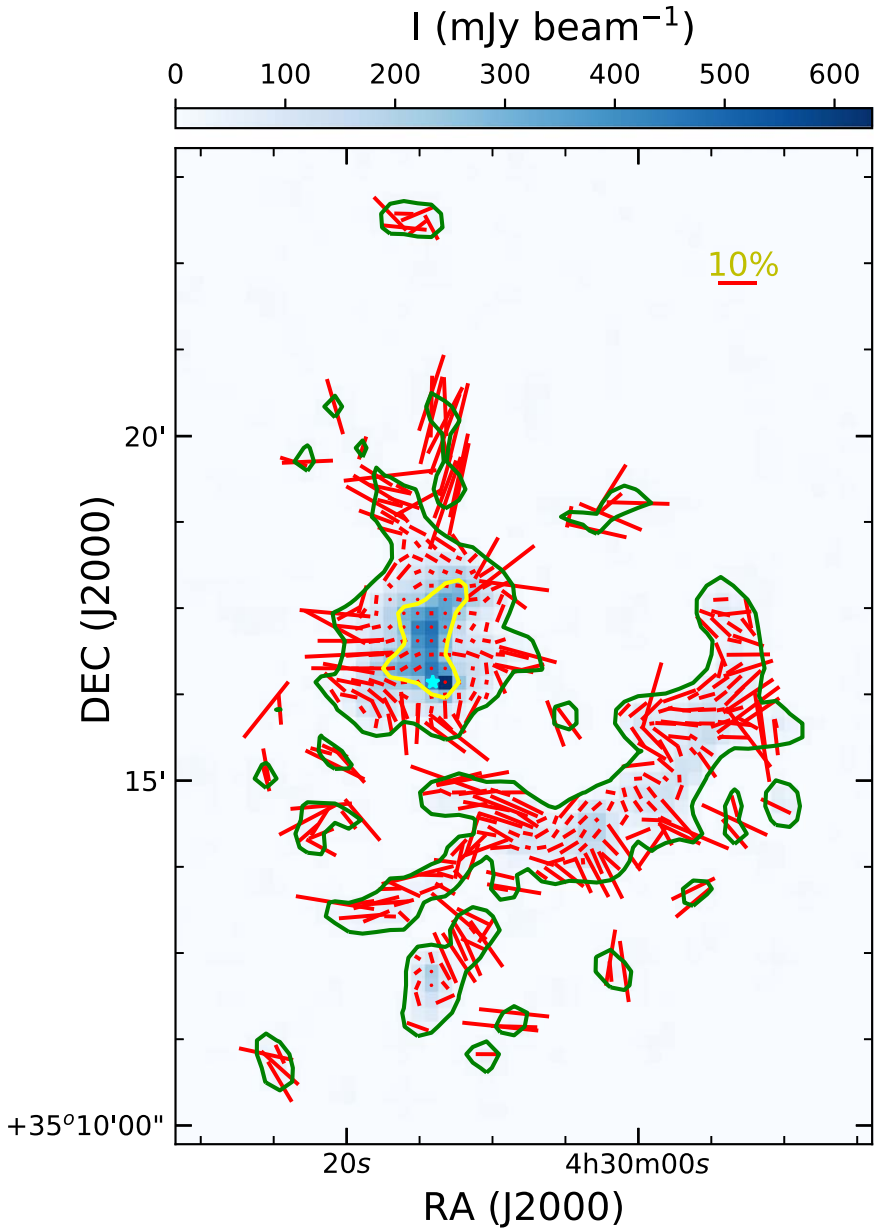

Figure 13. Same as Figure 5 but the length of the line segments is now proportional to the polarization fraction, $P(\%)$. A 10% line segment is shown for reference.

and $B_{\rm POS}$ is the strength in μG. As $B_{\rm POS}$ is the magnetic field component in the plane of the sky, a factor of 3 is introduced to correct for geometrical biases (Crutcher 2004).

Plugging $B_{\rm POS}$ and $N(H_2)$ obtained for the CR and the DL into Equation (12), we obtain λ for these regions, which are listed in Table 2.

The left panel of Figure 12 shows the measured values of $B_{\rm POS}$ as a function of the column density $N(H_2)$ for the different regions using the results from Table 2 together with those of previous studies (Pattle et al. 2017; Soam et al. 2018; Coudé et al. 2019; Soam et al. 2019; Wang et al. 2019) surveyed by POL-2. The dashed line corresponds to the separation between subcritical and supercritical regions. The line is obtained from Equation (12), setting $\lambda = 1$, where we have an equal contribution of mass and magnetic flux. Compared to other regions, LkHα 101 has particularly low values of $N(H_2)$. The Auriga–California region lies well above the dashed line, which is subcritical.

The right panel of Figure 12 shows the variation of $B_{\rm POS}$ with the mass-to-flux ratio, λ, for the different regions in the left panel. Compared to the other regions, the Auriga–California has a rather low value of λ and lies in the subcritical regime.

Being subcritical at the same time as being the densest region of Auriga–California may help to explain the very low star formation efficiency in comparison with that of the OMC as discussed in Section 1.

However, the star formation efficiency of a cloud depends on several parameters other than λ, such as matter distribution, evolutionary stage, and turbulence. More detailed studies are required to understand why the star formation efficiency in Auriga–California is lower than that of the OMC. Moreover, the measured ratio of the turbulent component to the large-scale component of the magnetic field is $\delta B/B_0 \sim 0.3$, suggesting that the effect of B-fields is dominant over the turbulence in the region.

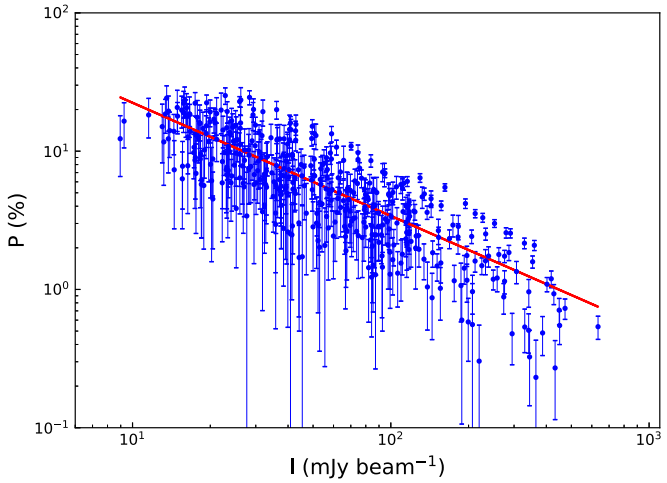

Figure 14. Dependence of polarization fraction on the total intensity. P tends to decrease with increasing I. The solid line is the best fit to a power-law function (see Section 4.4).

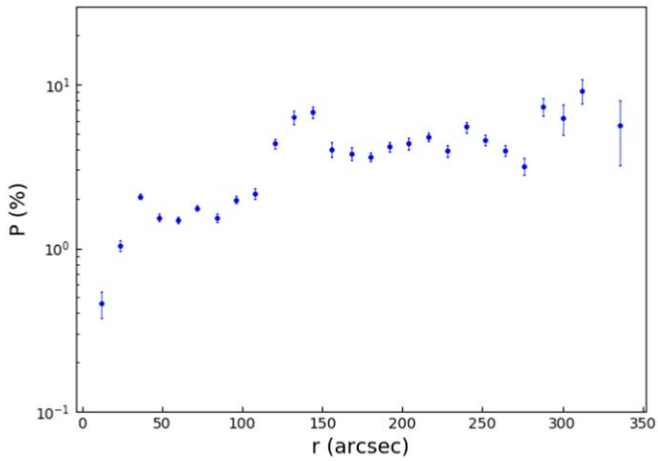

Figure 15. Dependence of P on the distance from LkHα 101. The polarization fraction decreases with r for $r < 150''$.

4.4. Dust Polarization and Grain Alignment

We now analyze the spatial variation of the polarization fraction within Auriga–California and explore grain alignment physics.

Figure 13 displays the map of the inferred magnetic line segments similar to Figure 5 but the length of the line segments is now proportional to the polarization fraction. It is clearly seen from the figure that the degree of polarization is higher in the more diffuse regions, but it drops significantly in the dense CR with maximum emission intensity (yellow contour). To see explicitly how the polarization fraction, P, changes with the total intensity I, in Figure 14 we show the variation of $P(\%)$ with I (the δP–$\delta\theta$ cut has been applied to the data). The observed polarization fraction tends to decrease with increasing total intensity, which is usually referred to as a polarization hole. A power-law fit of the form $P \propto I^{-\alpha}$ gives the power index $\alpha = 0.82 \pm 0.03$. The uncertainty in α is obtained from the fit and does not include systematic errors. The value of α found for the LkHα 101 region is in the expected range for molecular clouds, between 0.5 and 1. In other regions surveyed by BISTRO, the estimated values are $\alpha = 0.8$ for ρ Ophiuchus A (Kwon et al. 2018), 0.9 for ρ Ophiuchus B (Soam et al. 2018), 1.0 for ρ Ophiuchus C (Liu et al. 2019), and 0.9 for Perseus B1 (Coudé et al. 2019). Using a different approach working with non-debiased data, Pattle et al. (2019) found $\alpha = 0.34$ for Oph A and $\alpha = 0.6 - 0.7$ for Oph B and C, which are significantly smaller than those obtained by the previous authors.

We note that α is widely used as an indicator of dust grain alignment efficiency. One expects to have $\alpha = 0$ for constant efficiency of grain alignment and $\alpha = 1$ for grain alignment that only occurs in the outer layer of the cloud, with complete loss of grain alignment inside the cloud (Whittet et al. 2008). Various observations report the loss of grain alignment (i.e., $\alpha \sim 1$) at a large visual extinction of $A_V \sim 20$ toward starless cores (Alves et al. 2014; Jones et al. 2014; Santos et al. 2019), which is consistent with the prediction by RAT theory (Hoang et al. 2020). Therefore, the best-fit value $\alpha = 0.82$ here reveals that grain alignment still occurs inside the cloud, but with decreasing efficiency. This is consistent with the prediction from Radiative Torque (RAT) alignment theory (Lazarian & Hoang 2007; Hoang & Lazarian 2016) that grains inside the cloud can still be aligned due to stellar radiation from the LkHα 101 star.

Because LkHα 101 is the only early B star in the region, we display in Figure 15 the radial dependence of the polarization fraction averaged over $12''$ wide rings centered on the star. There is evidence for a rapid decrease of the polarization fraction at distances from the star smaller than $\sim 150''$. LkHα 101 is 15 times more massive than the Sun with a luminosity of 8×10^3 $L_\odot$ (Herbig et al. 2004). The angular distance from LkHα 101 at which the mean energy density in empty space is equal to that of the interstellar radiation field, 2.19×10^{-12} erg cm^{-3} (Draine 2010), is $\sim 3300''$. This distance is significantly larger than the distance where we find P to decrease.

To better understand the decreasing feature of P, in particular, the drastic decrease at $r < 150''$, we study the behavior of the polarization fraction P, column density $N(H_2)$, and dust temperature T_{dust} as a function of distance r from LkHα 101. The two latter quantities are taken from Herschel (Harvey et al. 2013). The upper-left panel of Figure 16 shows the dust temperature map overlaid by 850 μm emission. Figure 16 (upper right) shows the observational data (symbols) and our power-law fit, $P = ar^b$, with two slopes of $b = 0.86 \pm 0.04$ for $r < 130''$ and $b = 0.35 \pm 0.05$ for $r > 130''$. Here, the radius $r \sim 130''$ is chosen to be similar to the location of the separation between the CR and the DL (the valley in $N(H_2)$ versus r at $r \sim 130''$ in Figure 16, lower right). For the outer region ($r > 130''$), the polarization degree decreases slowly with decreasing r, which implies a slow decline in the grain alignment efficiency. However, the polarization degree decreases rapidly when approaching the location of LkHα 101 for $r < 130''$, whereas T_{dust} increases as expected from stronger heating by the star (Figure 16, lower left), except for only two data points close to the star at $r < 25''$ with decreased T_{dust}. Note that LkHα 101 is located at the location of the highest column density (Figure 16, lower right; for the column density map, see Figure 9).

In theory, the rapid decrease of P for $r < 130''$ can arise from (1) significant loss of grain alignment, and (2) strong variation of the magnetic field. According to the popular RAT alignment theory (Lazarian & Hoang 2007; Hoang & Lazarian 2016), the loss of grain alignment is induced by the decrease of the incident radiation field that can align grains and/or the increase of the gas density that enhances grain randomization. In our situation, grains are subject to increasing radiation flux from the LkHα 101 star

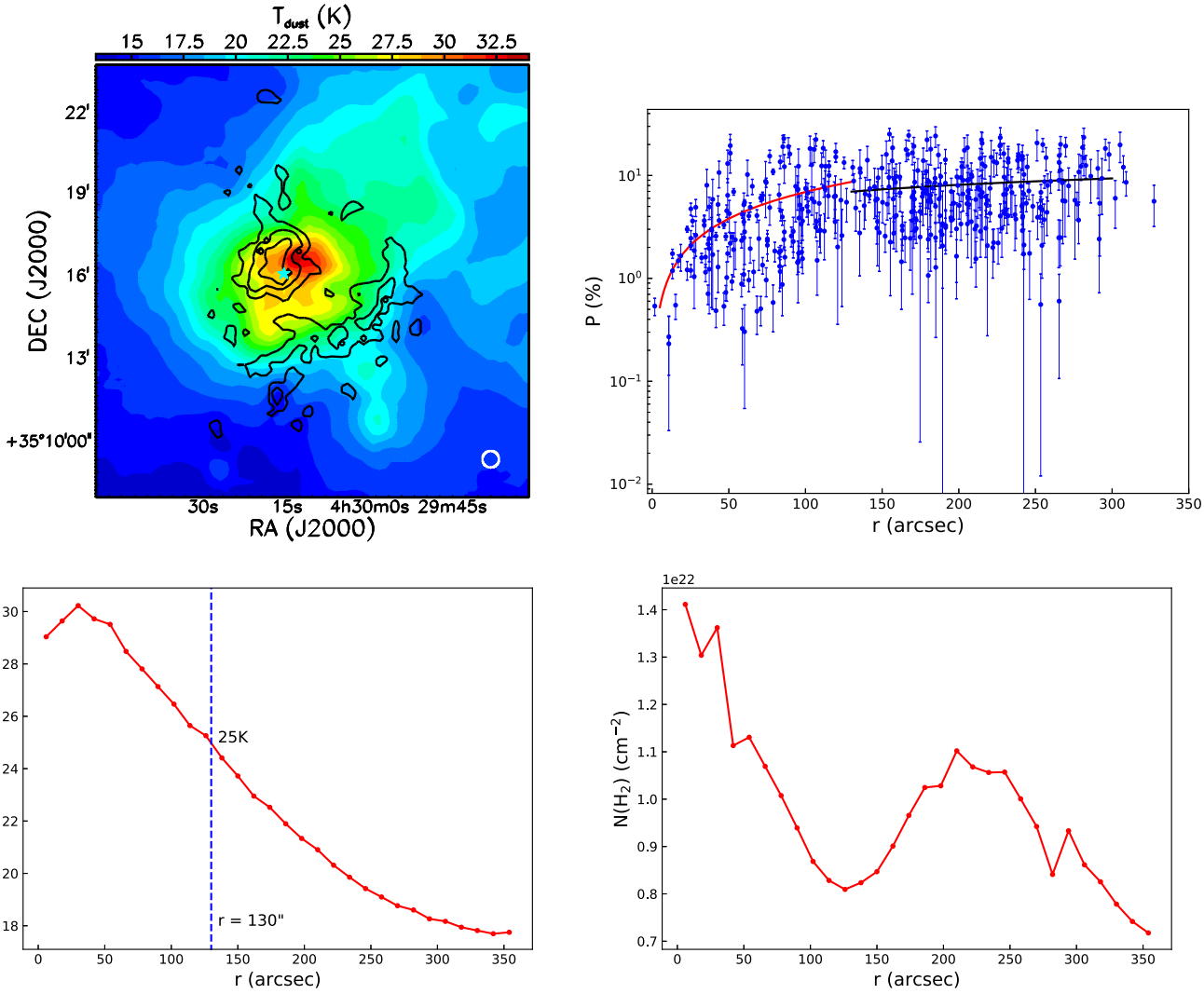

Figure 16. Upper-left panel: dust temperature map (color scale) overlaid by the 850 μm emission (contours). The Herschel beam size (36.″6) is shown in the lower-right corner of the map. The location of the early B star, LkHα 101, is at the cyan star marker. Upper-right panel: dependence of P on r. The r dependence of P is fitted to a power-law function for $r < 130''$ (red curve) and $r > 130''$ (black curve; see text). Lower-left panel: dependence of $T_{\rm dust}$ on r. The blue vertical dashed line shows the distance, $r = 130''$, from the star at which the average dust temperature is ∼25 K. Lower-right panel: dependence of $N(H_2)$ on r.

when r decreases, and the gas density of $n(H_2) \sim 10^4$ cm^{-3} in the CR is not very high. As a result, the degree of grain alignment is expected to increase with increasing local radiation energy density described by $T_{\rm dust}$ (Hoang et al. 2020), which would result in the increase of dust polarization (Lee et al. 2020). Therefore, the rapid decline of P for $r < 130''$ (Figure 16, upper right), or $T_{\rm dust} > 25$ K (Figure 16, lower left), may challenge the popular theory of grain alignment based on RATs.

Recently, Hoang et al. (2019) suggested that RATs from an intense radiation field can spin grains up to extremely fast rotation. As a result, centrifugal stress can exceed the maximum tensile strength of grain material, resulting in the disruption of large grains into smaller fragments. A detailed modeling of grain disruption toward a dense cloud with an embedded source is presented in Hoang et al. (2020). Because such large grains dominate dust polarization at far-IR/submillimeter, the degree of dust polarization is found to decrease with increasing local radiation energy density (Lee et al. 2020). For the hydrogen density of $n(H_2) \sim 10^4$ cm^{-3} listed in Table 2, the numerical modeling in Lee et al. (2020) implies that the polarization degree first increases with grain temperature due to the increase of the radiation flux, then it decreases when $T_{\rm dust}$ exceeds ∼25 K. This can explain the decrease of P at small r (or high $T_{\rm dust}$) observed in Figure 16. We note that previous observations by Planck (Guillet et al. 2018) and SOFIA/HAWC+ (Tram et al. 2021) also report the decrease of P when $T_{\rm dust}$ exceeds some value, which were explained by means of rotational disruption by RATs. A detailed modeling to understand the dependence of P versus r is beyond the scope of this paper.

The tangling of magnetic fields is usually invoked to explain the decrease of the polarization fraction, P, with the emission intensity, I, or column density (usually referred to as a polarization hole; see Pattle & Fissel 2019 for a review). However, there is no quantitative study that addresses the role of field tangling in causing the polarization holes at the scales of JCMT observations (or at smaller scales, i.e., CARMA[87]/SMA[88] and ALMA[89]). The fact that we observe relatively

[87] Combined Array for Research in Millimeter-wave Astronomy.
[88] Submillimeter Array.
[89] Atacama Large Millimeter/submillimeter Array.

ordered B-field in the region supports the RATD effect but cannot rule out the role of the field tangling. Single-dish versus interferometric observations of class 0 protostellar cores frequently show ordered fields on multiple spatial scales, even if the fields have very different morphologies on large (JCMT $\sim$ 10,000 au resolution) and small (ALMA $\sim$ 100 au resolution) scales. JCMT, CARMA, and ALMA maps of Serpens emb 8 (Hull et al. 2017a) and Serpens SMM1 (Hull et al. 2017b) show ordered fields on all scales. The case of SMM1 is particularly striking, where a well-ordered east–west field at JCMT scales (at least on the outskirts of the location of SMM1) is seen, and then a very well-ordered field north–south at CARMA scales, and then a highly complex field with multiple plane-of-sky components at ALMA scales. There are several other examples (see Sadavoy et al. 2018a, 2018b on IRAS 16293 and VLA 1623).

Analyses of the Planck polarization data (in particular, Planck Collaboration et al. 2015 and Planck Collaboration 2020) found that the polarization hole effect can be attributed entirely to turbulent tangling of the magnetic field along the line of sight and that the dust grain alignment efficiency is constant across a wide range of column densities. However, those spatial scales tend to be significantly larger than what we are dealing with in BISTRO observations. Similar conclusions are also reached in work performing similar statistical analyses of ALMA data, at spatial scales closer to the JCMT scales (Le Gouellec et al. 2020).

In summary, polarization holes have been observed in many star-forming regions (see Pattle & Fissel 2019). In the absence of field tangling, polarization holes observed toward protostars are inconsistent with the RAT alignment theory but can be explained by the joint effect of grain alignment and rotational disruption by RATs. There are several possible solutions that are being explored to explain the polarization holes, including RATD, magnetic field tangling. Detailed modeling of dust polarization taking into account grain alignment, disruption, and realistic magnetic fields is required to understand the origins of the polarization hole.

5. Conclusions

Using POL-2, we have measured the morphology and strength of the magnetic field of the LkHα 101 region for the first time. While the magnetic field is generally parallel to the filamentary structure of the DL, it is quite complex in the CR. In low-density clumps, in particular the elongated ones, the field is more aligned with the matter structure. The field strength is $\sim$91 μG for the CR and $\sim$138 μG for the DL. The polarization angle dispersions obtained from both unsharp masking and structure-function methods are in good agreement.

HARP data are used to evaluate the velocity dispersion of the regions, which show that the redshifted component of the cloud matches the region where we observed dust polarization; it matches the DL particularly well.

The power-law index of the dependence of the polarization fraction on total intensity was found to be 0.82 ± 0.03, which is in the expected range for molecular clouds. The mass-to-magnetic-flux-ratios in units of the critical value are $\lambda = 0.27$ for the CR and $\lambda = 0.30$ for the DL, smaller than unity and the smallest among regions surveyed by POL-2. The regions are subcritical, i.e., the B-fields are strong enough to be able to resist gravitational collapse. The ratio of the turbulent field to the underlying field $\delta B/B_0 \sim 0.3$ means that the underlying field dominates over the turbulent field. LkHα 101 is the densest region of Auriga–California. This gives supporting arguments for the low star-forming efficiency of Auriga–California in comparison with, in particular, the OMC. However, further study is required to explain the contrasting star formation efficiency of the AMC and the OMC.

Finally, we found that the polarization fraction decreases with increasing proximity to the B star, LkHα 101, which is also the highest density region of the observed field. This effect is similar to many previous observations. The rapid decrease of P with distance from the only B star in the region for $r < 130''$ is inconsistent with the popular RAT alignment theory but could be explained by the joint effect of grain alignment and rotational disruption by RATs. Other effects such as the geometry of the magnetic fields due to turbulence could potentially explain the polarization hole. More studies are required to understand the nature of polarization holes.

The James Clerk Maxwell Telescope is operated by the East Asian Observatory on behalf of The National Astronomical Observatory of Japan, Academia Sinica Institute of Astronomy and Astrophysics in Taiwan, the Korea Astronomy and Space Science Institute, the National Astronomical Observatories of China, and the Chinese Academy of Sciences (grant No. XDB09000000), with additional funding support from the Science and Technology Facilities Council of the United Kingdom and participating universities in the United Kingdom and Canada. Additional funds for the construction of SCUBA-2 and POL-2 were provided by the Canada Foundation for Innovation. The data taken in this paper were observed under project code M16AL004. We thank Ngan Le for contributions to this work in its earlier phase. We are grateful to Prof. Pierre Darriulat and other VNSC/DAP members for their useful comments and discussions. This research is funded by the Vietnam National Foundation for Science and Technology Development (NAFOSTED) under grant No. 103.99-2019.368. T.H. acknowledges the support by the National Research Foundation of Korea (NRF) grant funded by the Korea government (MSIT) through the Mid-career Research Program (2019R1A2C1087045). C.L.H.H. acknowledges the support of the NAOJ Fellowship and JSPS KAKENHI grants 18K13586 and 20K14527. J.D.F. and D.J. are supported by the National Research Council of Canada and by individual NSERC Discovery Grants. C.W.L. is supported by the Basic Science Research Program through the National Research Foundation of Korea (NRF) funded by the Ministry of Education, Science and Technology (NRF-2019R1A2C1010851). M.T. is supported by JSPS KAKENHI grant Nos. 18H05442,15H02063, and 22000005. J.K. is supported JSPS KAKENHI grant No.19K14775. A.S. acknowledges the support from the NSF through grant AST-1715876. W.K. was supported by the New Faculty Startup Fund from Seoul National University. H.-W.Y. acknowledges support from Ministry of Science and Technology (MOST) grant MOST 108-2112-M-001-003-MY2 in Taiwan. H.L.L. acknowledges funding from a Fondecyt Postdoctoral project (code 3190161). F.K. and L.F. acknowledge support from the Ministry of Science and Technology of Taiwan, under grant MoST107-2119-M-001-031-MY3 and from Academia Sinica under grant AS-IA-106-M03. The authors wish to recognize and acknowledge the very significant cultural role and reverence that the summit of Maunakea has

always had within the indigenous Hawaiian community. We are most fortunate to have the opportunity to conduct observations from this mountain.

Software: Starlink (Currie et al. 2014), Astropy (Robitaille et al. 2013; Price-Whelan et al. 2018).

Facility: James Clerk Maxwell Telescope (JCMT).

Appendix
Characteristics of the Raw Data

Figure A1 displays the week correlations of δI vs. $\delta\theta$, δPI vs. $\delta\theta$, δI vs. δP, and δPI vs. δP. Figure A2 displays the distributions of I, PI, P, δI, δPI, δP, θ, and $\delta\theta$ for the raw data set, namely no cut has been applied. Their respective means and rms values are listed in Table A1. Note that the presence of a P value larger than 100% is caused by noise in PI and I (i.e., random noise spikes can result in PI being larger than I). The total number of pixels containing data, namely pixels having $I > 0$ and $PI > 0$ and $P > 0$, is 1466 out of $90 \times 90 = 8100$ pixels of the whole map.

The mean uncertainties of the polarization angle of $\langle\delta\theta\rangle \sim 16°$ is average in comparison with other regions surveyed by BISTRO. It is better for Orion with $\langle\delta\theta\rangle \sim 4°$, Perseus B1 with $\langle\delta\theta\rangle \sim 6°$, IC 5146 with $\langle\delta\theta\rangle \sim 9°$, Ophiuchus A with $\delta\theta < 12°$, but worse for Ophiuchus B and C with $20° < \delta\theta < 80°$ and $12° < \delta\theta < 47°$, respectively. The main factors dictating the precision of the polarization angle measurements are the weather conditions and whether the region has bright polarized emission. Our observed region is rather polarization-faint. We note that $\langle\delta\theta\rangle$ for the sources mentioned here are calculated with some data selection criteria, which naturally bring the value of $\langle\delta\theta\rangle$ down. For example, in the case of Orion, only pixels having $P/\delta P > 5$ were kept. From the right panel of the upper row of the same figure, we can see from the distribution of P that there are a number of pixels having $P > 100\%$, which is unphysical. Investigating these pixels in more detail, we find that most of the pixels come from low-emission regions where the edge effect—high noise at the edges of the map—is important (Figure A3 left). Moreover, they have small values of I (0.93, 0.79) mJy beam^{-1} and PI (2.08, 1.02) mJy beam^{-1} (Figure A3 center) as well as

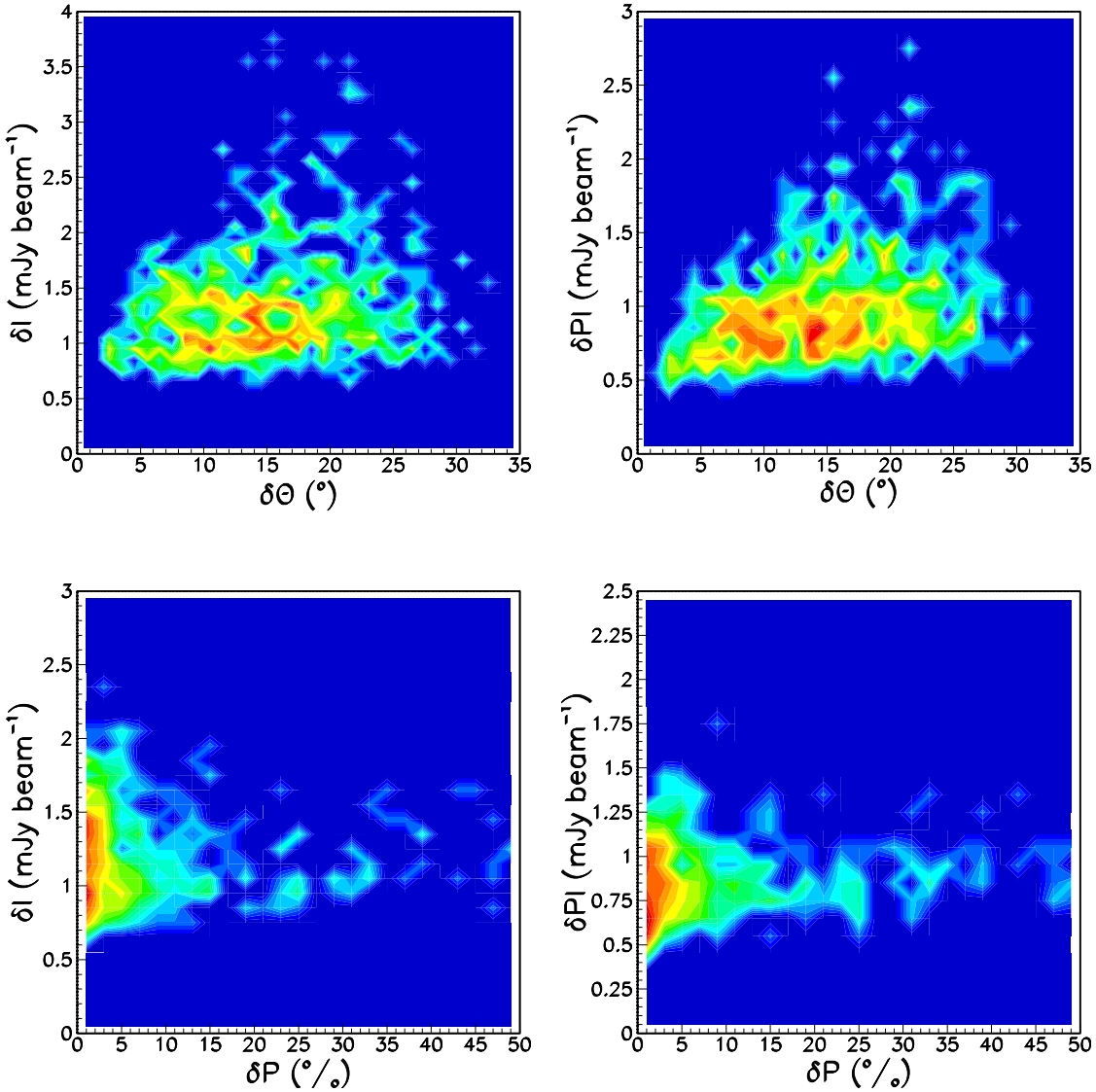

Figure A1. Correlations of measurement uncertainties from left to right, top to bottom (the color represents the number of data points in logarithmic scales): δI vs. $\delta\theta$, δPI vs. $\delta\theta$, δI vs. δP, and δPI vs. δP.

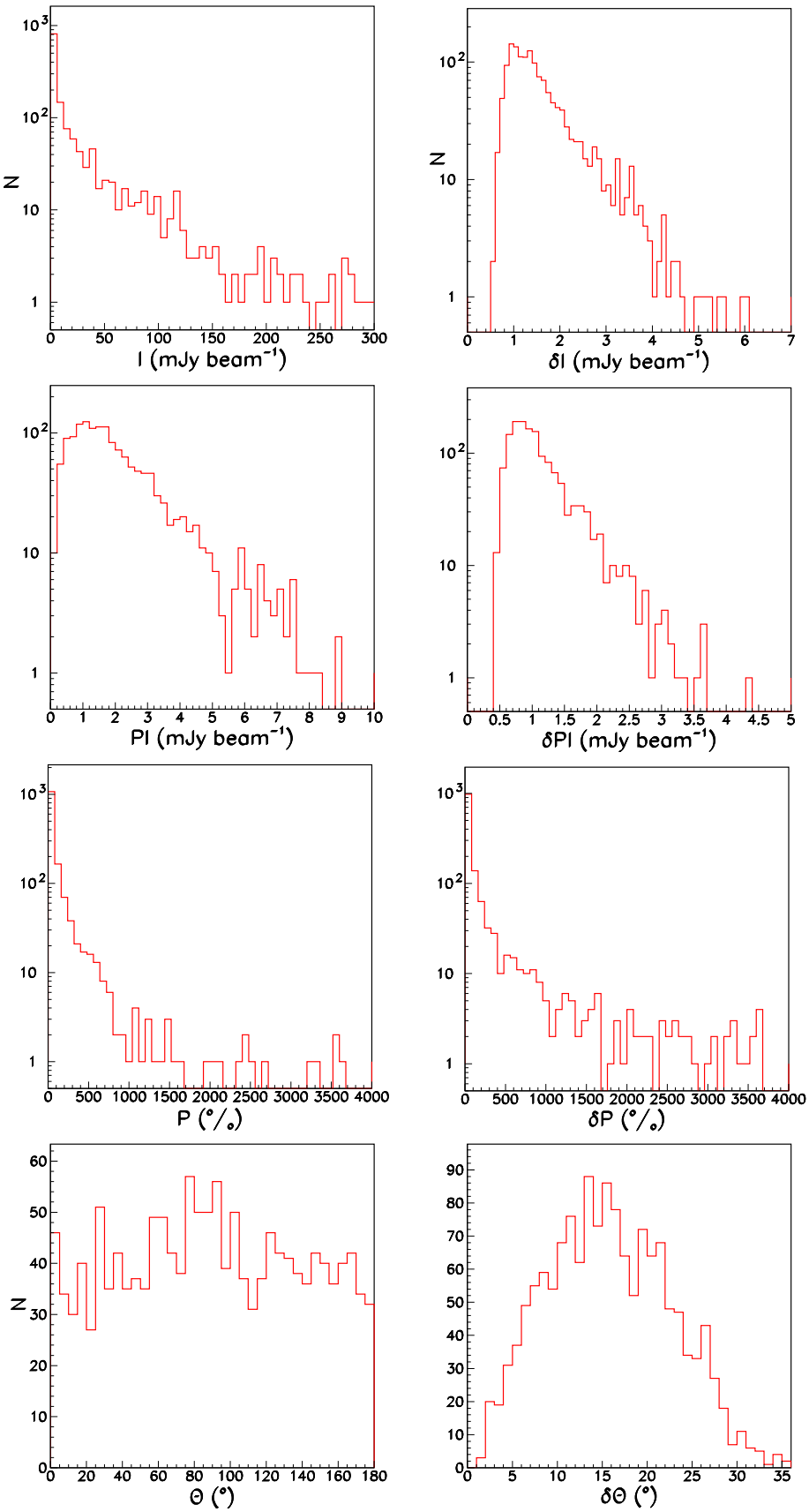

Figure A2. From left to right, top to bottom: distributions of I, δI, PI, δPI, P, δP, θ, and $\delta\theta$.

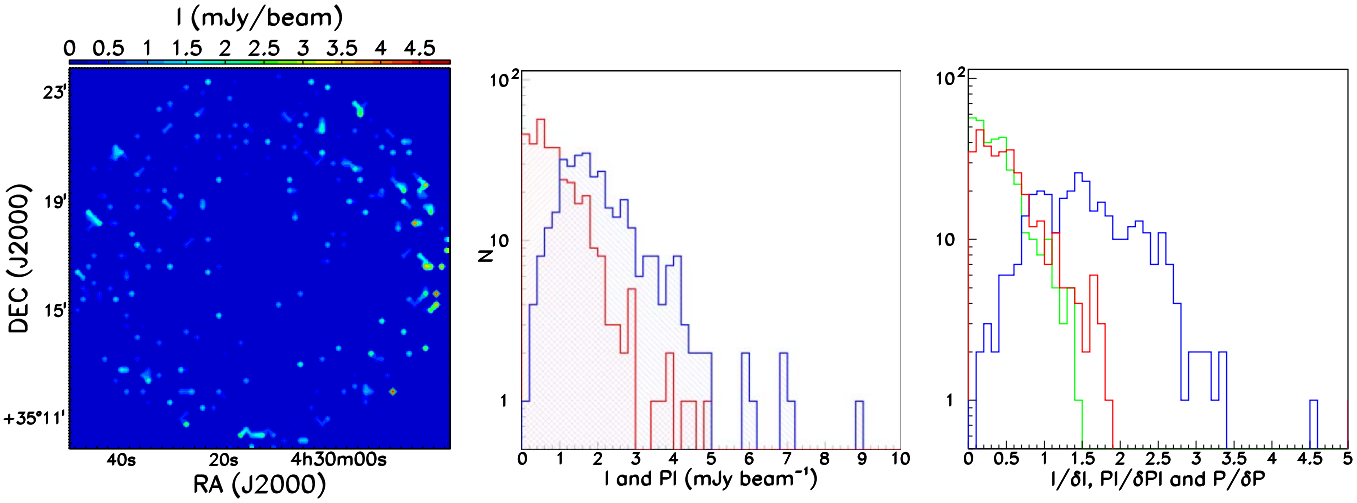

Figure A3. Bad pixels (pixels having $P > 100\%$ due to low S/N or having short exposure time). Left: I map; center: distributions of I (red) and PI (blue); right: distributions of $I/\delta I$ (red), $PI/\delta PI$ (blue), $P/\delta P$ (green). Bad pixels are located at the map edges (left) and have low I, PI (center), and low S/N (right).

Table A1
Means and rms Values of I, δI, PI, δPI, P, δP, θ, and $\delta\theta$

	I (mJy beam^{-1})	δI (mJy beam^{-1})	PI (mJy beam^{-1})	δPI (mJy beam^{-1})	P (%)	δP (%)	θ (°)	$\delta\theta$ (°)
Mean	24.2	1.6	2.0	1.1	129.2	220.6	89.6	15.7
rms	44.2	0.8	1.5	0.5	311.4	524.0	50.2	6.8

S/Ns whose means and rms are (0.53, 0.40) for $I/\delta I$, (1.55, 0.67) for $PI/\delta PI$, and (0.40, 0.32) for $P/\delta P$ itself (Figure A3 right). This result is expected and due to errors on polarization fraction (Figure A2 middle right) being Ricean, rather than Gaussian distributed (Pattle et al. 2019). In POL-2 observations, the central 3′radius region is designed to have a flat S/N and coverage drops off sharply towards the map edges at a radius of 6′ (Friberg et al. 2016).

ORCID iDs

Nguyen Bich Ngoc https://orcid.org/0000-0002-5913-5554
Pham Ngoc Diep https://orcid.org/0000-0002-2808-0888
Harriet Parsons https://orcid.org/0000-0002-6327-3423
Kate Pattle https://orcid.org/0000-0002-8557-3582
Thiem Hoang https://orcid.org/0000-0003-2017-0982
Derek Ward-Thompson https://orcid.org/0000-0003-1140-2761
Le Ngoc Tram https://orcid.org/0000-0002-6488-8227
Charles L. H. Hull https://orcid.org/0000-0002-8975-7573
Mehrnoosh Tahani https://orcid.org/0000-0001-8749-1436
Ray Furuya https://orcid.org/0000-0003-0646-8782
Pierre Bastien https://orcid.org/0000-0002-0794-3859
Keping Qiu https://orcid.org/0000-0002-5093-5088
Woojin Kwon https://orcid.org/0000-0003-4022-4132
Yasuo Doi https://orcid.org/0000-0001-8746-6548
Shih-Ping Lai https://orcid.org/0000-0001-5522-486X
Simon Coudé https://orcid.org/0000-0002-0859-0805
Tao-Chung Ching https://orcid.org/0000-0001-8516-2532
Jihye Hwang https://orcid.org/0000-0001-7866-2686
Archana Soam https://orcid.org/0000-0002-6386-2906
Jia-Wei Wang https://orcid.org/0000-0002-6668-974X
Tyler L. Bourke https://orcid.org/0000-0001-7491-0048
Do-Young Byun https://orcid.org/0000-0003-1157-4109
Huei-Ru Vivien Chen https://orcid.org/0000-0002-9774-1846
Zhiwei Chen https://orcid.org/0000-0003-0849-0692
Wen Ping Chen https://orcid.org/0000-0003-0262-272X
Jungyeon Cho https://orcid.org/0000-0003-1725-4376
Antonio Chrysostomou https://orcid.org/0000-0002-9583-8644
Eun Jung Chung https://orcid.org/0000-0003-0014-1527
James Di Francesco https://orcid.org/0000-0002-9289-2450
David Eden https://orcid.org/0000-0002-5881-3229
Chakali Eswaraiah https://orcid.org/0000-0003-4761-6139
Lapo Fanciullo https://orcid.org/0000-0001-9930-9240
Laura M. Fissel https://orcid.org/0000-0002-4666-609X
Erica Franzmann https://orcid.org/0000-0003-2142-0357
Per Friberg https://orcid.org/0000-0002-8010-8454
Rachel Friesen https://orcid.org/0000-0001-7594-8128
Gary Fuller https://orcid.org/0000-0001-8509-1818
Tim Gledhill https://orcid.org/0000-0002-2859-4600
Sarah Graves https://orcid.org/0000-0001-9361-5781
Qilao Gu https://orcid.org/0000-0002-2826-1902
Jennifer Hatchell https://orcid.org/0000-0002-4870-2760
Martin Houde https://orcid.org/0000-0003-4420-8674
Shu-ichiro Inutsuka https://orcid.org/0000-0003-4366-6518
Kazunari Iwasaki https://orcid.org/0000-0002-2707-7548
Doug Johnstone https://orcid.org/0000-0002-6773-459X
Ji-hyun Kang https://orcid.org/0000-0001-7379-6263
Sung-ju Kang https://orcid.org/0000-0002-5004-7216
Miju Kang https://orcid.org/0000-0002-5016-050X
Akimasa Kataoka https://orcid.org/0000-0003-4562-4119
Koji Kawabata https://orcid.org/0000-0001-6099-9539
Francisca Kemper https://orcid.org/0000-0003-2743-8240
Kee-Tae Kim https://orcid.org/0000-0003-2412-7092
Jongsoo Kim https://orcid.org/0000-0002-1229-0426
Tae-Soo Pyo https://orcid.org/0000-0002-3273-0804

Lei Qian https://orcid.org/0000-0003-0597-0957
Ramprasad Rao https://orcid.org/0000-0002-1407-7944
John Richer https://orcid.org/0000-0002-9693-6860
Anna Scaife https://orcid.org/0000-0002-5364-2301
Gwanjeong Kim https://orcid.org/0000-0003-2011-8172
Shinyoung Kim https://orcid.org/0000-0001-9333-5608
Kyoung Hee Kim https://orcid.org/0000-0001-9597-7196
Mi-Ryang Kim https://orcid.org/0000-0002-1408-7747
Florian Kirchschlager https://orcid.org/0000-0002-3036-0184
Jason Kirk https://orcid.org/0000-0002-4552-7477
Masato I. N. Kobayashi https://orcid.org/0000-0003-3990-1204
Patrick M. Koch https://orcid.org/0000-0003-2777-5861
Vera Konyves https://orcid.org/0000-0002-3746-1498
Takayoshi Kusune https://orcid.org/0000-0002-9218-9319
Jungmi Kwon https://orcid.org/0000-0003-2815-7774
Kevin Lacaille https://orcid.org/0000-0001-9870-5663
Sang-Sung Lee https://orcid.org/0000-0002-6269-594X
Yong-Hee Lee https://orcid.org/0000-0001-6047-701X
Chin-Fei Lee https://orcid.org/0000-0002-3024-5864
Jeong-Eun Lee https://orcid.org/0000-0003-3119-2087
Hyeseung Lee https://orcid.org/0000-0003-3465-3213
Chang Won Lee https://orcid.org/0000-0002-3179-6334
Di Li https://orcid.org/0000-0003-3010-7661
Hua-bai Li https://orcid.org/0000-0003-2641-9240
Hong-Li Liu https://orcid.org/0000-0003-3343-9645
Junhao Liu https://orcid.org/0000-0002-4774-2998
Tie Liu https://orcid.org/0000-0002-5286-2564
Sheng-Yuan Liu https://orcid.org/0000-0003-4603-7119
Xing Lu https://orcid.org/0000-0003-2619-9305
A-Ran Lyo https://orcid.org/0000-0002-9907-8427
Steve Mairs https://orcid.org/0000-0002-6956-0730
Masafumi Matsumura https://orcid.org/0000-0002-6906-0103
Brenda Matthews https://orcid.org/0000-0003-3017-9577
Gerald Moriarty-Schieven https://orcid.org/0000-0002-0393-7822
Fumitaka Nakamura https://orcid.org/0000-0001-5431-2294
Nagayoshi Ohashi https://orcid.org/0000-0003-0998-5064
Takashi Onaka https://orcid.org/0000-0002-8234-6747
Geumsook Park https://orcid.org/0000-0001-8467-3736
Yoshito Shimajiri https://orcid.org/0000-0001-9368-3143
Hiroko Shinnaga https://orcid.org/0000-0001-9407-6775
Motohide Tamura https://orcid.org/0000-0002-6510-0681
Ya-Wen Tang https://orcid.org/0000-0002-0675-276X
Xindi Tang https://orcid.org/0000-0002-4154-4309
Kohji Tomisaka https://orcid.org/0000-0003-2726-0892
Serena Viti https://orcid.org/0000-0001-8504-8844
Hongchi Wang https://orcid.org/0000-0003-0746-7968
Anthony Whitworth https://orcid.org/0000-0002-1178-5486
Hsi-Wei Yen https://orcid.org/0000-0003-1412-893X
Hyunju Yoo https://orcid.org/0000-0002-8578-1728
Chuan-Peng Zhang https://orcid.org/0000-0002-4428-3183
Philippe André https://orcid.org/0000-0002-3413-2293
Sven van Loo https://orcid.org/0000-0003-4746-8500

References

Alves, F., Frau, P., Girart, J. M., et al. 2014, A&A, 569, L1
Alves, J., Zucker, C., Goodman, A. A., et al. 2020, Natur, 578, 237
Andersson, B., Lazarian, A., & Vaillancourt, J. E. 2015, ARA&A, 53, 501
André, P., Francesco, J. D., Ward-Thompson, D., et al. 2014, in Protostars and Planets VI, ed. H. Beuther et al. (Tucson, AZ: Arizona), 27
Bohlin, R. C., Savage, B. D., & Drake, J. F. 1978, ApJ, 224, 132
Broekhoven-Fiene, H., Matthews, B. C., Harvey, P., et al. 2018, ApJ, 852, 73
Buckle, J. a., Hills, R., Smith, H., et al. 2009, MNRAS, 399, 1026
Chandrasekhar, S., & Fermi, E. 1953, ApJ, 118, 116
Chapin, E. L., Berry, D. S., Gibb, A. G., et al. 2013, MNRAS, 430, 2545
Coudé, S., Bastien, P., Houde, M., et al. 2019, ApJ, 877, 88
Crutcher, R. M. 2004, Ap&SS, 292, 225
Crutcher, R. M. 2012, ARA&A, 50, 29
Currie, M., Berry, D., Jenness, T., et al. 2014, ASPC, 485, 391
Davis, L. 1951, Phys. Rev., 81, 890
Doi, Y., Hasegawa, T., Furuya, R. S., et al. 2020, ApJ, 899, 28
Draine, B. T. 2010, Physics of the Interstellar and Intergalactic Medium (Princeton, NJ: Princeton Univ. Press)
Friberg, P., Bastien, P., Berry, D., et al. 2016, Proc. SPIE, 9914, 991403
Friberg, P., Berry, D., Savini, G., et al. 2018, Proc. SPIE, 10708, 107083M
Gaia Collaboration 2018, A&A, 616, A1
Guillet, V., Fanciullo, L., Verstraete, L., et al. 2018, A&A, 610, A16
Hall, J. S., & Mikesell, A. H. 1949, AJ, 54, 187
Harvey, P. M., Fallscheer, C., Ginsburg, A., et al. 2013, ApJ, 764, 133
Herbig, G., Andrews, S. M., & Dahm, S. 2004, ApJ, 128, 1233
Hildebrand, R. H. 1988, QJRAS, 29, 327
Hildebrand, R. H., Kirby, L., Dotson, J. L., Houde, M., & Vaillancourt, J. E. 2009, ApJ, 696, 567
Hiltner, W. 1949, Natur, 163, 283
Hoang, T., & Lazarian, A. 2016, ApJ, 831, 159
Hoang, T., Tram, L. N., Lee, H., & Ahn, S.-H. 2019, NatAs, 3, 766
Hoang, T., Tram, L. N., Lee, H., Diep, P. N., & Ngoc, N. B. 2020, arXiv:2010.07742
Holland, W., Bintley, D., Chapin, E., et al. 2013, MNRAS, 430, 2513
Hull, C. L., Mocz, P., Burkhart, B., et al. 2017a, ApJL, 842, L9
Hull, C. L., Girart, J. M., Tychoniec, Ł., et al. 2017b, ApJ, 847, 92
Inoue, T., & Inutsuka, S.-i. 2012, ApJ, 759, 35
Jones, T., Bagley, M., Krejny, M., Andersson, B.-G., & Bastien, P. 2014, AJ, 149, 31
Kwon, J., Doi, Y., Tamura, M., et al. 2018, ApJ, 859, 4
Lada, C. J., Lombardi, M., & Alves, J. F. 2009, ApJ, 703, 52
Lazarian, A. 2007, JQSRT, 106, 225
Lazarian, A., & Hoang, T. 2007, MNRAS, 378, 910
Le Gouellec, V., Maury, A., Guillet, V., et al. 2020, A&A, 644, A11
Lee, H., Hoang, T., Le, N., & Cho, J. 2020, ApJ, 896, 44
Li, D. L., Esimbek, J., Zhou, J.-J., et al. 2014, A&A, 567, A10
Liu, J., Qiu, K., Berry, D., et al. 2019, ApJ, 877, 43
Matthews, T. G., Ade, P. A. R., Angilè, F. E., et al. 2014, ApJ, 784, 116
Montier, L., Plaszczynski, S., Levrier, F., et al. 2015a, A&A, 574, A135
Montier, L., Plaszczynski, S., Levrier, F., et al. 2015b, A&A, 574, A136
Omodaka, T., Nagayama, T., & Dobashi, K. 2020, PASJ, 72, 55
Ostriker, E. C., Stone, J. M., & Gammie, C. F. 2001, ApJ, 546, 980
Palmeirim, P., André, P., Kirk, J., et al. 2013, A&A, 550, A38
Pattle, K., & Fissel, L. 2019, FrASS, 6, 15
Pattle, K., Ward-Thompson, D., Berry, D., et al. 2017, ApJ, 846, 122
Pattle, K., Ward-Thompson, D., Hasegawa, T., et al. 2018, ApJL, 860, L6
Pattle, K., Lai, S.-P., Hasegawa, T., et al. 2019, ApJ, 880, 27
Pillai, T. G. S., Clemens, D. P., Reissl, S., et al. 2020, NatAs, 4, 1195
Planck Collaboration 2020, A&A, 641, A12
Planck Collaboration, Ade, P. A. R., Aghanim, N., et al. 2015, A&A, 576, A104
Planck Collaboration, Ade, P. A. R., Aghanim, N., et al. 2016, A&A, 586, A138
Price-Whelan, A. M., Sipőcz, B., Günther, H., et al. 2018, AJ, 156, 123
Robitaille, T. P., Tollerud, E. J., Greenfield, P., et al. 2013, A&A, 558, A33
Sadavoy, S. I., Myers, P. C., Stephens, I. W., et al. 2018a, ApJ, 859, 165
Sadavoy, S. I., Myers, P. C., Stephens, I. W., et al. 2018b, ApJ, 869, 115
Santos, F. P., Chuss, D. T., Dowell, C. D., et al. 2019, ApJ, 882, 113
Serkowski, K. 1962, AdA&A, 1, 289
Soam, A., Pattle, K., Ward-Thompson, D., et al. 2018, ApJ, 861, 65
Soam, A., Liu, T., Andersson, B., et al. 2019, AJ, 883, 95
Soler, J. D., Ade, P. A. R., Angilè, F. E., et al. 2017, A&A, 603, A64
Soler, J. D., Hennebelle, P., Martin, P. G., et al. 2013, ApJ, 774, 128
Tahani, M., Plume, R., Brown, J. C., & Kainulainen, J. 2018, A&A, 614, 100A
Tram, L. N., Hoang, T., Lee, H., et al. 2021, ApJ, 906, 115
Wang, J.-W., Lai, S.-P., Eswaraiah, C., et al. 2019, AJ, 876, 42
Ward-Thompson, D., Pattle, K., Bastien, P., et al. 2017, ApJ, 842, 66
Whittet, D. C. B., Hough, J. H., Lazarian, A., & Hoang, T. 2008, ApJ, 674, 304
Zhang, G. Y., André, P., Men'shchikov, A., & Wang, K. 2020, A&A, 642, A76
Zucker, C., Speagle, J. S., Schlafly, E. F., et al. 2020, A&A, 633, A51